Modelling adhesive wear extension in fretting interfaces: An advection-dispersion-reaction contact oxygenation approach

Soha Baydoun, Pierre Arnaud, Siegfried Fouvry

Modelling adhesive wear extension in fretting interfaces: An advection-dispersion-reaction contact oxygenation approach

Soha Baydoun[a]*, Pierre Arnaud[b]*, Siegfried Fouvry[a]*

[a]Ecole Centrale de Lyon, LTDS Laboratory, 36 av Guy de Collongue, 69130 Ecully, France

[b]CentraleSupelec, MSSMAT Laboratory, 8-10 rue Joliot Curie, 91190 Gif-sur-Yvette, France

*Corresponding authors email addresses: soha.baydoun@ec-lyon.fr (S. Baydoun), pierre.arnaud@centralesupelec.fr (P. Arnaud) and siegfried.fouvry@ec-lyon.fr (S. Fouvry)

Abstract

This paper aims at modelling contact oxygenation concept (COC) which describes the effects of fretting loading conditions on di-oxygen flow within the interface and the associated partition between abrasive and adhesive wear domains in fretting wear scars. This is achieved by modelling oxygen transport within fretting interface using an advection-dispersion-reaction approach (ADR) by considering debris bed as a compact porous medium traversed by atmospheric gases. ADR model is calibrated using three fretting tests of flat-on-flat 34NiCrMo16 interface. Results show that ADR approach can predict the partition of abrasion and adhesion for wide range of sliding frequencies, normal forces and contact sizes. Besides, it can capture the transition of wear mechanisms from pure abrasive to mixed abrasive-adhesive wear at different loading conditions.

Key words: Fretting wear; Contact oxygenation concept; Abrasive-adhesive wear; Advection-Dispersion-Reaction model (ADR).

1. Introduction

Fretting is experienced in contacts submitted to normal load and undergoing micro-displacement oscillatory motion [1,2]. Many investigations underline that fretting degradations are highly influenced by the sliding condition operating in the interface. For very small displacement, a partial slip condition involving an inner stuck domain surround by sliding areas is observed inducing fatigue and cracking mechanisms. By applying larger displacement amplitudes, the contact shifts toward a gross slip sliding condition where the high friction energy dissipated in the interface promotes surface wear by debris formation and debris ejection. In both partial and gross slip conditions, the displacement amplitude is relatively small so that most of the contact area is concealed from the outer environment.

The response of the material under gross slip fretting is governed by the activated wear mechanisms at the interface. These mechanisms were classified by Tabor [3] into three categories: adhesive, abrasive, and a composite adhesive-abrasive wear. Adhesive wear takes place whenever two virgin surfaces mechanically contact and bond each other [4]. On the other hand, abrasive wear takes place if a hard asperity or particle cuts one of the sliding surfaces [3]. This results in material removal by plowing or gouging instead of sticking or being pulled of as in the case of adhesion [5]. During fretting, abrasive wear usually interacts with surface corrosion which results in creation of oxide films. Composite wear is defined as a mixture of adhesive and abrasive-oxidative wear which is the case of most sliding interfaces [3]. It is characterized by presence of metal surfaces covered by thin oxide films where abrasive-oxidative wear is predominant. On the other hand, adhesive wear prevails when metal-metal contact takes place generating

hard tribologically transformed structures (TTS) [6–8]. The transition in wear mechanisms under fretting loadings can be clarified by the “Contact Oxygenation Concept” (COC) which was proposed by Fouvry and co-authors [9] as a general description of the effect of “air distilling” and “oxygen exclusion” within the interface which were formerly observed by Mary et al. [10] and Shipway and co-workers [11–13].

Contact oxygenation concept (COC) describes the evolution of the interfacial di-oxygen partial pressure “P_{O_2}” within fretting contacts and the associated partition of abrasion and adhesion zones under different loading parameters (Fig. 1). Indeed, surface oxidation generated by fretting triggers the consumption of the diffusing dioxygen molecules from the outer environment and consequently the reduction of P_{O_2} towards the center of the interface. However, if the di-oxygen partial pressure exceeds a threshold value “$P_{O_2,th}$” over the entire contact area, full contact oxygenation marked by abrasive-oxidational wear prevails. On the other side of the coin, an abrasive-adhesive wear manifests itself in case of partial contact oxygenation such that adhesion and metal transfer are detected in the locations where the oxygen supply is below $P_{O_2,th}$ (Fig. 1). Following this premise, “oxygen distance d_O” parameter can be introduced as the distance from the interface boundaries to the frontiers of adhesion zone after which oxygen supply becomes very limited (Fig. 1).

It was shown that “oxygen distance d_O” is highly dictated by the operating loading conditions in the interface namely the sliding frequency and the contact pressure [14]. In fact, when the latter are relatively low, abrasive-oxidational wear dominates. In contrary, when the contact pressure and the sliding frequency are high, composite adhesive-abrasive wear is triggered (Fig. 1). However, the other loading conditions such as the

number of fretting cycles, sliding amplitude, contact size and contact orientation appeared to have no substantial effect on oxygen distance at least in the studied ranges. Hence, a parametric model linking oxygen distance evolution to the contact pressure and sliding frequency was proposed. Although the aforesaid model was highly predictive, it remained parametric in essence, hence more physical interpretation is sought.

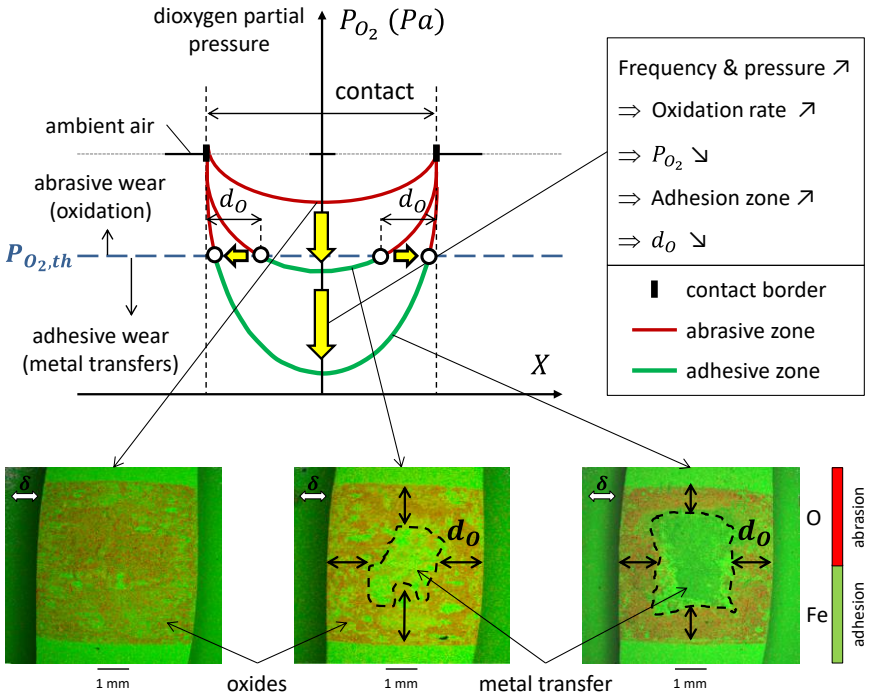

Fig. 1. Description of the contact oxygenation concept (COC) that illustrates the evolution of the oxygen distance d_O and the associated extension of adhesion and abrasion domains observed on a flat-on-flat 34NiCrMo16 fretting wear interface [14].

In the light of the former results, the purpose of this research work is to explain and model contact oxygenation and the evolution of oxygen distance observed in fretting contacts. This is achieved by modelling oxygen transport using an advection-dispersion-

reaction approach by considering debris bed as compact powdery porous medium traversed by atmospheric gases. Fig. 2 illustrates the principle of this model which is based on establishing the balance between the di-oxygen flow coming from the external part of the contact through an advection-dispersion process within the porous debris layer, and the oxygen consumption rate induced by the oxidation reaction of the fresh metal surface exposed by the friction process (i.e. removing the protective oxide layer through asperities interactions).

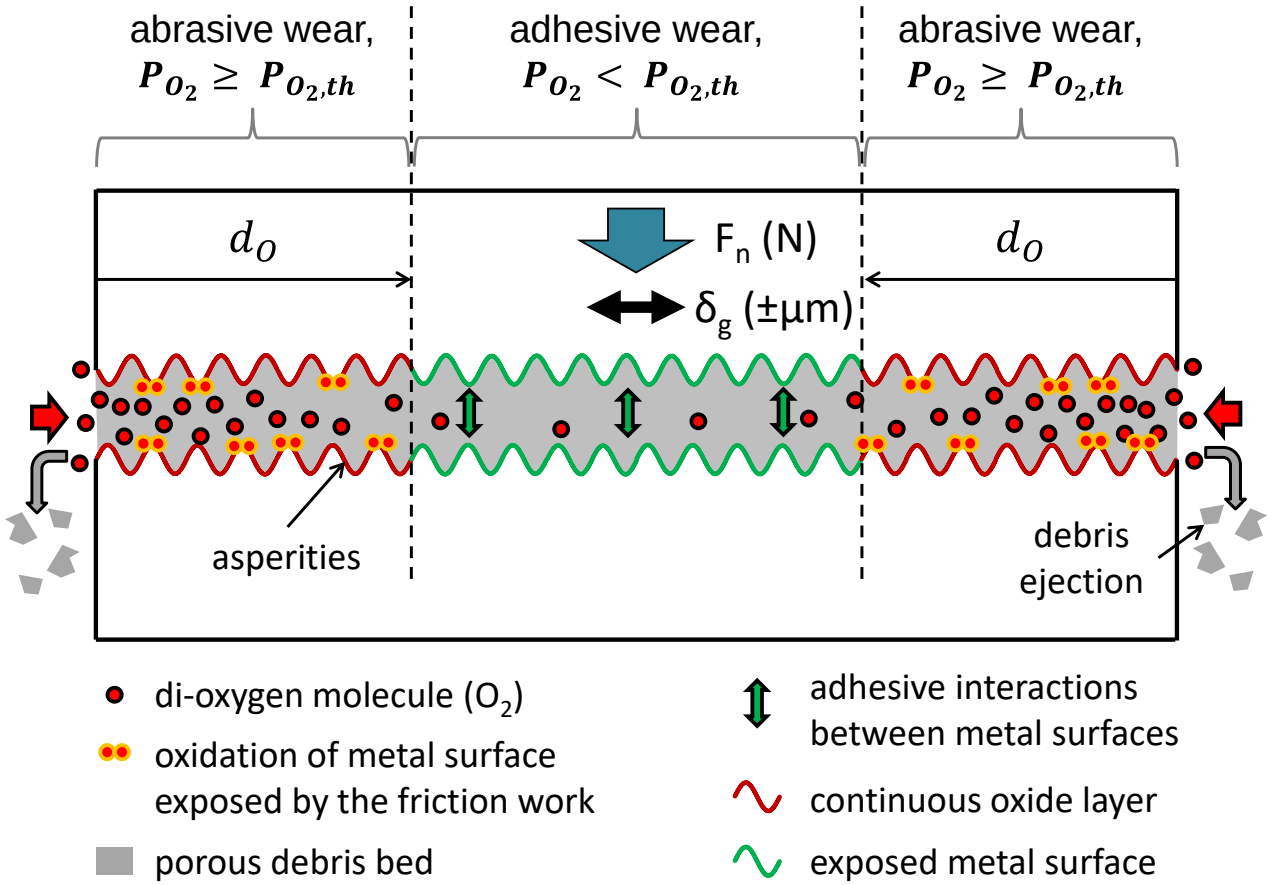

Fig. 2. Illustration of the ADR model to predict the extension of adhesive / abrasive wear distribution within a fretting interface.

As detailed previously, abrasive-oxidational wear dominates the regions where oxygen concentration is sufficiently high (i.e., $P_{O_2} \geq P_{O_2,th}$) whereas adhesive wear is detected whenever oxygen access becomes restricted such that $P_{O_2} < P_{O_2,th}$. The oxygen distance "d_O" marks the transition between these two wear phenomena. Hence, this paper will detail the basics of the model, the various hypotheses involved and the related numerical scheme to predict the relative partition between abrasive and adhesive wear zones (i.e. oxygen distance d_O). The given predictions are discussed regarding the corresponding experiments thus establishing the potential but also the limits of this multi-physics strategy to predict wear processes partition within fretting interfaces.

2. ADR model

In ADR model, debris bed is considered to be a dry compact powdery porous medium allowing transport of gases (Fig. 3). This model includes only two gas components which are nitrogen and oxygen. The other gases in the atmosphere (mainly argon, water vapor, and carbon dioxide) are neglected firstly because they present around 1% of the atmospheric air which is nearly negligible compared to other gas constituents. Secondly, these gases do not play a significant role in oxidation and consequently contact oxygenation whenever oxygen concentration is relatively high. This is confirmed by previous studies showing that high temperature oxidation of steel in gases containing free oxygen is chiefly governed by the oxygen gas which is the main oxidizing agent and that the additions of CO_2 and H_2O (with relatively high percentages compared to the air composition) had little effect on the magnitude of the initial oxidation rates [15]. Besides, the overall oxidation in atmospheres containing higher free oxygen content (>15 %) was shown to be unaffected by changing the concentration of H_2O or CO_2 [16]. This is further

confirmed by fretting wear tests of steel alloy where water vapor and carbon dioxide seemed to have negligible effect on the oxidized debris whenever when the oxygen concentration is sufficient (>2%) [17].

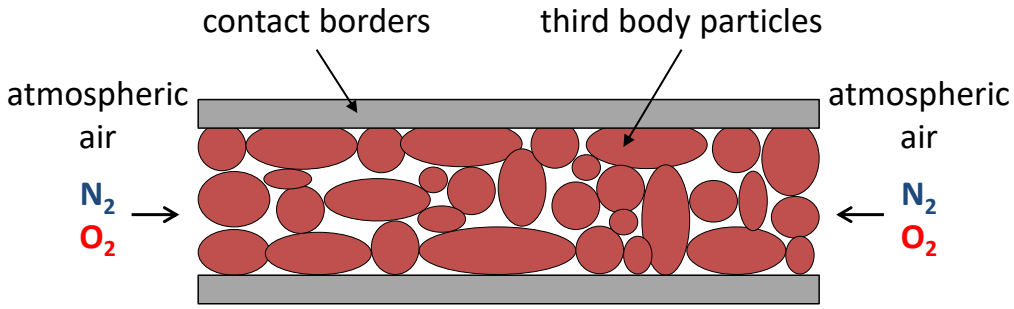

Fig. 3. Schematic presentation of the powdery porous debris bed allowing gas transport.

2.1 Gas transport in debris bed

Gas transport in porous media is chiefly controlled by dispersion and advection [18]. Hence, for a gas component "i" the general flux equation is given by:

$$J_i = J_{a,i} + J_{d,i} \quad (1)$$

With J_i being the general molar flux of gas component i (mol.m^{-2}.s^{-1}), $J_{a,i}$ the advective flux of gas component i (mol.m^{-2}.s^{-1}) and $J_{d,i}$ the dispersive flux of gas component i (mol.m^{-2}.s^{-1}).

2.1.1 Advective transport

The advection (bulk flow) (Eq. 2) is the transport of the entire gas mixture by bulk motion due to gradients in the total pressure of the gas mixture.

$$J_{a,i} = vC_i \quad (2)$$

With C_i being the molar concentration of a component i (mol.m^{-3}), and v being the advection velocity of the gas mixture in the debris bed (m.s^{-1}).

Gas advection in porous media is investigated using Darcy's law [19] which defines gas advection velocity "v" as being directly proportional to the gas phase pressure gradients [20]. The pressure gradients are caused by compositional changes in the gas mixture which, in fretting wear, are caused by the consumption of oxygen during oxidation reaction of freshly exposed metal. Darcy's law is given by:

$$v = -\frac{k}{\mu}\nabla P \tag{3}$$

With μ being the gas mixture viscosity (kg.m^{-1}.s^{-1}), k the intrinsic permeability of the debris bed (m^2), and P being the total pressure of the gas mixture (Pa).

The total pressure P of a gas mixture of "m" gases is equal to the sum of the partial pressures of the individual gases (P_i) according to Dalton's law [21]:

$$P = \sum_{i=1}^{m} P_i \tag{4}$$

The viscosity (μ) of the entire gas mixture is estimated using Wilke model [22] through applying a mixing rule for the viscosities of the individual gases based on kinetic gas theory.

$$\mu = \sum_{i=1}^{m} \frac{\mu_i}{1 + \sum_{j=1,\, j\neq i}^{m} \theta_{i,j}\, \frac{y_j}{yi}} \tag{5}$$

$$\theta_{i,j} = \frac{\left[1 + \left(\frac{\mu_i}{\mu_j}\right)^{1/2} \times \left(\frac{M_j}{M_i}\right)^{1/4}\right]^2}{\sqrt{8}\left(1 + \frac{M_i}{M_j}\right)^{1/2}} \quad (6)$$

$$y_i = \frac{n_i}{\sum_{i=1}^{m} n_i} = \frac{P_i}{\sum_{i=1}^{m} P_i} \quad (7)$$

With μ being the viscosity of the gas mixture (kg.m^{-1}.s^{-1}), μ_i the viscosity of the gas component "i" (kg.m^{-1}.s^{-1}), y_i the mole fraction of gas component "i", n_i the number of moles of gas component "i", $\theta_{i,j}$ is expressed in Eq. 6, and M_i is the molar mass of gas component "i" (kg.mol^{-1}).

The intrinsic permeability can be estimated using Carman-Kozeny equation [23,24]:

$$k = \frac{{d_p}^2 a^3}{180(1-a)^2} \quad (8)$$

With d_p is the average particle size in the debris bed (m²) and a is the porosity of the debris bed (dimensionless).

2.1.2 Dispersive transport

Dispersion of gases constitutes of diffusive and mechanical mixing processes [25]. Diffusive flux is governed by molecular diffusion which is defined as the random spreading of a gas component "i" in a mixture of gases due to concentration gradients [25]. Mechanical mixing is a solute-independent constituent of dispersion controlled by the physical characteristics of the porous medium and the carrier gas velocity [25]. Mechanical mixing and dilution of gases result from velocity variations that originate from non-uniform velocity profiles within a single pore due to wall-effects, pore size

distributions (large pores induce higher velocities than smaller ones), and the tortuosity effects [25].

Dispersion is analyzed using Fick's law [26] which relates the dispersive flux of gases to the concentration gradients:

$$J_{d,i} = -D_i \nabla C_i \tag{9}$$

The dispersion coefficient of a gas component "i" (D_i) is given by [25]:

$$D_i = D_{mechanical\ mixing} + D_{diffusion,i} \tag{10}$$

The molecular diffusion term of dispersion is solute dependent and is given by [25]:

$$D_{diffusion,i} = \tau D_{im} \tag{11}$$

The diffusion coefficient of a gas component "i" diffusing in a homogeneous mixture of "m" gases [18] is given by Wilke model [27] such that:

$$D_{im} = \frac{1 - y_i}{\sum_{j=1,\, i \neq j}^{m} \frac{y_j}{D_{ij}}} \tag{12}$$

Where D_{ij} is the diffusion coefficient for a binary mixture of gas components "i" and "j" ($m^2.s^{-1}$) which can be estimated using a semi-empirical model proposed by Chen and Othmer [28]:

$$D_{i,j} = \frac{0.604 \times 10^{-8} \times T^{1.81} \times \left(\frac{M_i + M_j}{M_i \times M_j}\right)^{0.5}}{P \times \left(T_{C,i} \times T_{C,j}\right)^{0.1405} \times \left(V_{C,i}^{0.4} + V_{C,j}^{0.4}\right)^2} \tag{13}$$

With M_i being the molar mass of a gas component "i" (kg.mol^{-1}), $T_{C,i}$ the critical temperature (K), $V_{C,i}$ the critical volume (m^3.kmol^{-1}), T the desired air temperature (K), and P being the air pressure (bar).

The product of the diffusion coefficient and the tortuosity "τ" is referred to as "effective diffusion coefficient, "$D_{diffusion,i}$" [25]. The tortuosity is an intrinsic property of a porous medium estimated from the ratio of the actual length of the flow path to the straight-line distance between its ends [29]. Indeed, in porous media the diffusion coefficient of a given gas is less than that in free air due to the presence of the solid phase which decreases the cross-sectional area allowing diffusion in addition to the tortuosity effects [18,25]. Several authors attempted to empirically and semi-empirically express tortuosity "τ" as a function of the porosity "Φ" and the volumetric air content "a". Moldrup et al. [30] model (Eq. 14) will be considered in this investigation. This latter diffusion-based model is widely used in literature and is selected here as it was shown to most accurately predict tortuosity for both dry and moist porous media [31–33].

$$\tau = 0.66\Phi \left(\frac{a}{\Phi}\right)^2 \quad (14)$$

In case of dry porous medium the porosity is assumed to be equal to the volumetric air content ($\Phi = a \Rightarrow \tau = 0.66a$).

The mechanical mixing term of dispersion is solute independent and is given by [25]:

$$D_{mechanical\ mixing} = \alpha_L |v| \quad (15)$$

Where v is Darcy's velocity (m.s^{-1}) and α_L is the longitudinal dispersivity of the gas mixture which is a measure of the physical heterogeneity of the porous medium (in m)

[25]. The variable α_L can be empirically correlated to the scale length or the distance travelled by the gas which is, in the current case, equal to the contact size "L" expressed in meters. One of the aforesaid empirical relations is that proposed by Pickens and Grisak [34] as follows:

$$\alpha_L = \frac{L}{10} \tag{16}$$

Note that transverse dispersion is also observed in porous media and is expressed by transverse dispersivity coefficient "α_T". Nevertheless, transverse dispersion is very small compared to the longitudinal dispersion (by factor 10) for this reason it will be neglected in the current study (i.e. $\alpha_T \approx 0$) [25].

2.2 Reaction term

In fact, the oxidation of Iron (Fe) during fretting wear presents a cardinal sink for oxygen gas. Di-oxygen molecules react with iron (Fe) element to form hematite (Fe_2O_3) and magnetite (Fe_3O_4) oxides. This oxidation reaction (i.e. consumption of O_2) depends on the concentration of di-oxygen molecules (C_{O_2}) but also on the material properties and the contact sliding conditions which monitor the progressive elimination of the protective oxide layer exposing new fresh metal surfaces to react with the available di-oxygen molecules. For simplicity and as a first approach, a first-order decay rate of oxygen gas is assumed such that:

$$R_{O_2} = -r_{O_2} \times C_{O_2} \tag{17}$$

where r_{O_2} (s^{-1}) is the oxidation rate coefficient which expresses the reaction rate between the fresh metal surface and the available dioxygen molecules in the interfacial air. It

depends on the fretted material and its avidity to react with oxygen but also on the formed protective oxide layer (i.e. limiting the oxidation of the metal) and its endurance regarding friction processes. The r_{O_2} reaction rate coefficient mainly depends on tribological parameters like the contact pressure, sliding amplitude, and frequency. The explicit formulation of r_{O_2} is quite complex. However, stating that the higher the friction power dissipated in the interface, the faster the metal reaction with the available oxygen gas, a simple phenomenological empirical expression based on the so-called "p.v" power factor (with "p" being the pressure and "v" being the sliding speed) will be considered. The proposed formulation and its calibration are detailed later in section 4.4. Note that the given formulation neglects the reactivity with nitrogen gas (i.e. $r_{N_2} \approx 0$) although some nitriding processes could be observed [9,35] as detailed in the following discussion (Section 6).

2.3 ADR continuity equation

The continuity equation of the advection-dispersion-reaction (ADR) process of a gas constituent "i" is therefore given by:

$$a\frac{dC_i}{dt} = -\nabla.(J_i) + R_i = -\nabla.(-D_i\nabla C_i + vC_i) + R_i \tag{18}$$

By multiplying Eq. 18 by "$R.T$" following ideal gas law [36] (Eq. 19), continuity equation can be expressed in terms of the partial pressure of individual gas components instead of the molar concentrations (Eq. 20).

$$P_i = C_i.R.T \tag{19}$$

$$a\frac{dP_i}{dt} = -\nabla.(-D_i\nabla P_i + vP_i) + R_i \quad (20)$$

with R being the universal gas constant (8.314 J.mol^{-1}.K^{-1}) and T being the temperature (K).

3. Numerical solution of the ADR continuity equation

3.1 Finite difference scheme

So far, no analytical solution is found for ADR continuity equation with variable advection velocity and dispersion coefficients. Hence, the latter will be solved numerically by applying a finite difference scheme which was previously described by Stein and co-authors [18]. The nominal contact area "$A = L_x.L_y$" is discretized into equal number of nodes ($n_x = n_y$) in both directions such that gas partial pressures vary linearly between these nodes. Hence, the contact sizes L_x and L_y are respectively divided into p and q segments centered at the nodes yielding the continuity equation below:

$$a_{(p,q)}\frac{dP_{i\,(p,q)}}{dt} = \frac{J_{i\left(p-\frac{1}{2},q\right)} - J_{i\left(p+\frac{1}{2},q\right)}}{\Delta x} + \frac{J_{i\left(p,q-\frac{1}{2}\right)} - J_{i\left(p,q+\frac{1}{2}\right)}}{\Delta y} + R_i \quad (21)$$

The discretization of the time domain is expressed as follows:

$$\frac{P_{i\,(p,q)}^{j+1} - P_{i\,(p,q)}^{j}}{\Delta t} = \frac{J_{i\left(p-\frac{1}{2},q\right)} - J_{i\left(p+\frac{1}{2},q\right)}}{\Delta x.\,a_{(p,q)}} + \frac{J_{i\left(p,q-\frac{1}{2}\right)} - J_{i\left(p,q+\frac{1}{2}\right)}}{\Delta y.\,a_{(p,q)}} + \frac{R_i}{a_{(p,q)}} \quad (22)$$

$$P_{i\,(p,q)}^{j+1} = P_{i\,(p,q)}^{j} + \Delta t.\left(\frac{J_{i\left(p-\frac{1}{2},q\right)} - J_{i\left(p+\frac{1}{2},q\right)}}{\Delta x.\,a_{(p,q)}} + \frac{J_{i\left(p,q-\frac{1}{2}\right)} - J_{i\left(p,q+\frac{1}{2}\right)}}{\Delta y.\,a_{(p,q)}} + \frac{R_i}{a_{(p,q)}}\right) \quad (23)$$

$$P_{i\,(p,q)}^{j+1} = P_{i\,(p,q)}^{j} + \Delta t.\,f_{i\,(p,q)}^{j} \quad (24)$$

$for\ i \in [1,m]\ , p \in [1,n_x]\ , q \in [1,n_y]\ , j \in [0,n_t]$

The general flux of a gas component "i" is discretized through the lower boundaries (Eq. 25 & 27) and the upper boundaries (Eq. 26 & 28) of segments p and q respectively.

$$J_{i\left(p-\frac{1}{2}q\right)} = -\left[D_{i\left(p-\frac{1}{2},q\right)} \cdot \frac{P_{i\,(p,q)} - P_{i\,(p-1,q)}}{\Delta x}\right] - \left[\frac{k_{(p-\frac{1}{2},q)}}{\mu_{(p-\frac{1}{2},q)}} \cdot \frac{P_{(p,q)} - P_{(p-1,q)}}{\Delta x} \cdot \frac{P_{i\,(p,q)} + P_{i\,(p-1,q)}}{2}\right] \quad (25)$$

$$J_{i\left(p+\frac{1}{2},q\right)} = -\left[D_{i\left(p+\frac{1}{2},q\right)} \cdot \frac{P_{i\,(p+1,q)} - P_{i\,(p,q)}}{\Delta x}\right] - \left[\frac{k_{(p+\frac{1}{2},q)}}{\mu_{(p+\frac{1}{2},q)}} \cdot \frac{P_{(p+1,q)} - P_{(p,q)}}{\Delta x} \cdot \frac{P_{i\,(p+1,q)} + P_{i\,(p,q)}}{2}\right] \quad (26)$$

$$J_{i\left(p,q-\frac{1}{2}\right)} = -\left[D_{i\left(p,q-\frac{1}{2}\right)} \cdot \frac{P_{i\,(p,q)} - P_{i\,(p,q-1)}}{\Delta y}\right] - \left[\frac{k_{(p,q-\frac{1}{2})}}{\mu_{(p,q-\frac{1}{2})}} \cdot \frac{P_{(p,q)} - P_{(p,q-1)}}{\Delta y} \cdot \frac{P_{i\,(p,q)} + P_{i\,(p,q-1)}}{2}\right] \quad (27)$$

$$J_{i\left(p,q+\frac{1}{2}\right)} = -\left[D_{i\left(p,q+\frac{1}{2}\right)} \cdot \frac{P_{i\,(p,q+1)} - P_{i\,(p,q)}}{\Delta y}\right] - \left[\frac{k_{(p,q+\frac{1}{2})}}{\mu_{(p,q+\frac{1}{2})}} \cdot \frac{P_{(p,q+1)} - P_{(p,q)}}{\Delta y} \cdot \frac{P_{i\,(p,q+1)} + P_{i\,(p,q)}}{2}\right] \quad (28)$$

3.2 Solution method

The partial differential equation of the ADR model is solved using Runge-Kutta method with order 4 (RK4) which provides more stable and accurate solution than explicit Euler scheme even when a higher time step Δt (by factor 10) is considered. According to RK4, the initial value problem is firstly defined in Eq. 29 & 30 as follows:

$$\frac{dP_{i\,(p,q)}}{dt} = f^{j}_{i\,(p,q)} = f\left(t_j, P^{j}_{i\,(p,q)}\right) \quad (29)$$

$$P^{j=0}_{i\,(p,q)} = P^{0}_{i\,(p,q)} \quad (30)$$

Secondly, the four Runge-Kutta increments are determined following the equations below:

$$K_1 = \Delta t \times f\left(t_j, P^{j}_{i\,(p,q)}\right) \quad (31)$$

$$K_2 = \Delta t \times f\left(t_j + \frac{\Delta t}{2}, P^{j}_{i\,(p,q)} + \frac{K_1}{2}\right) \quad (32)$$

$$K_3 = \Delta t \times f\left(t_j + \frac{\Delta t}{2}, P_{i\,(p,q)}^{j} + \frac{K_2}{2}\right) \tag{33}$$

$$K_4 = \Delta t \times f\left(t_j + \Delta t, P_{i\,(p,q)}^{j} + K_3\right) \tag{34}$$

Thirdly, the partial pressure of gas "i" at node "(p,q)" can be estimated for a time step "$j+1$" by adding the gas pressure at the previous time step "j" to the weighted average of the four Runge-Kutta increments:

$$P_{i\,(p,q)}^{j+1} = P_{i\,(p,q)}^{j} + \frac{1}{6}(K_1 + 2K_2 + 2K_3 + K_4) \tag{35}$$

$$t_{j+1} = t_j + \Delta t \tag{36}$$

3.3 Steady-state solution

The steady-state solution is defined by a stopping criteria such that if the difference between the pressure profiles between two consecutive instants of time falls below a certain predefined value "ε", then the steady state is reached.

$$\left|P_i^{j+1} - P_i^{j}\right| < \varepsilon \;\Rightarrow steady\ state\ is\ reached \tag{37}$$

4. Parameters identification and model calibration

The input parameters related to the air conditions, gases physical properties, spatial and temporal discretization applied for the simulation of the steady-state condition are compiled in Table 1.

Table 1. Input parameters of ADR model.

Air conditions	T= 25°C=298 K		P=1 atm=1.01325 bar=101325 Pa		R= 8.314 J/K.mol	
Gas physical properties	Oxygen, O_2	$T_{C,O2}$=154.4 K	$P_{C,O2}$=50.43 bars	$V_{C,O2}$=0.08 m^3/kmol	M_{O2}=32 g/mol	μ_{O2}=20.8e-6 kg/m.s
	Nitrogen, N_2	$T_{C,N2}$=126 K	$P_{C,N2}$=34 bars	$V_{C,N2}$=0.089 m^3/kmol	M_{N2}=28 g/mol	μ_{N2}=17.9e-6 kg/m.s
Spatial discretization	n_x=50	n_y=50	Temporal discretization	Δt=0.00001 s	Steady state condition	ε=1e^{-5} Pa

Fig. 4 illustrates a global overview of the ADR flow chart. It also considers the necessity to develop an adequate strategy combining literature analysis and well-calibrated fretting experiments to identify the unknown parameters required by the model (Eq.18) which are respectively:

$P_{O_2,th}$: The threshold partial pressure below which the steel oxidation is no more possible and adhesive wear is activated.

$d_p, a, k,$ & α_L: The intrinsic properties of the porous debris layer.

r_{O_2} : The dioxygen reaction rate coefficient with fresh steel metal exposed by the friction process consuming the available dioxygen molecules present within the interface to generate metal oxides.

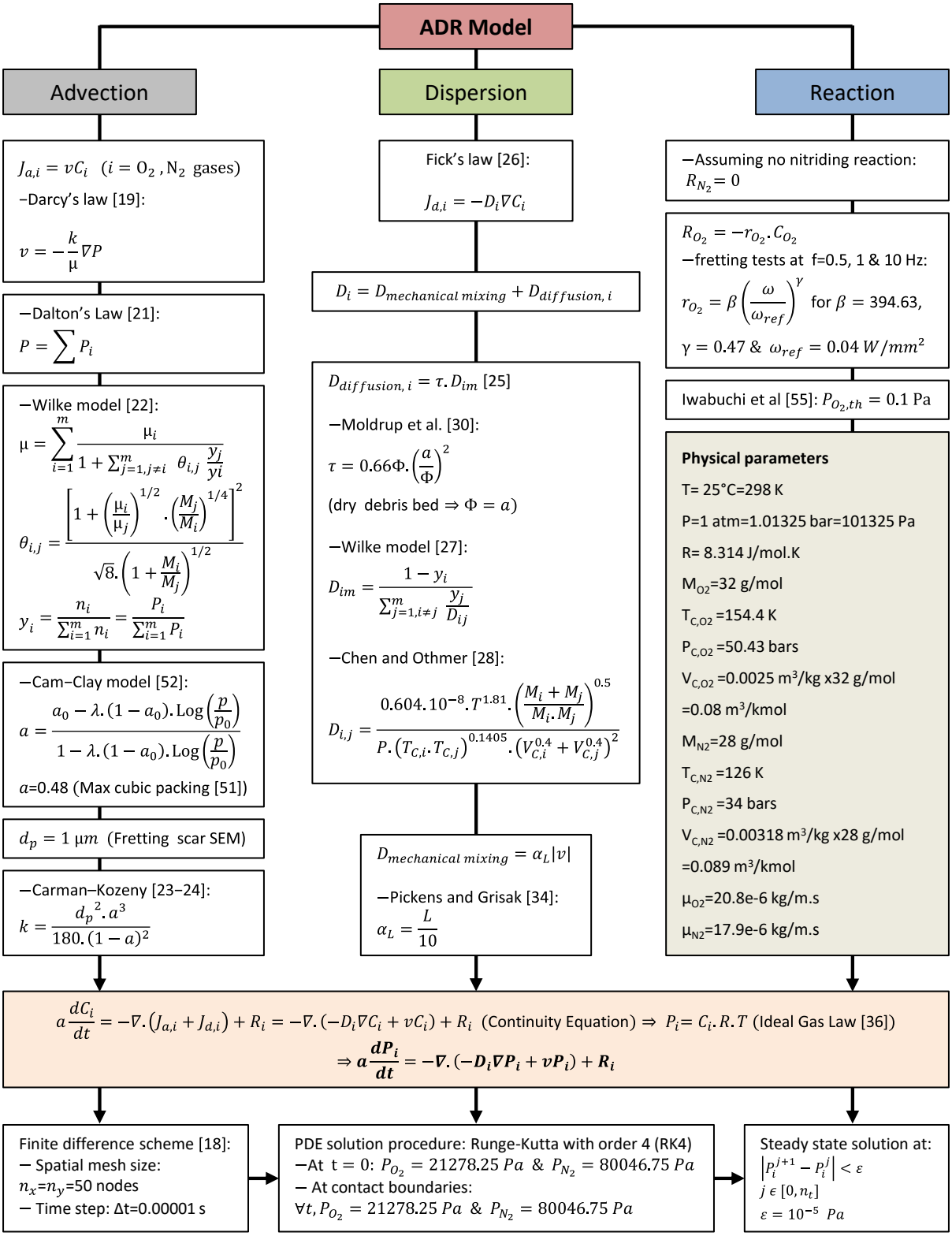

Fig. 4. Flow chart summarizing the input data, models and the numerical solution of the ADR model.

4.1 Illustration of the studied interface

Fretting tests were performed on a homogeneous 34NiCrMo16 interface. This low steel alloy was previously investigated in [14,37]. The mechanical properties and the chemical composition of 34NiCrMo16 are displayed in Table 2.

Table 2. Mechanical properties and chemical composition of 34NiCrMo16.

Mechanical properties of 34NiCrMo16 (documentation of material supplier [38])									
Young's modulus, E (GPa)		Poisson's ratio, ν		Yield stress (0.2%), $\sigma_{\gamma\,0.2\%}$ (MPa)			Ultimate stress, σ_u (MPa)		
205		0.3		950			1130		
Chemical composition of 34NiCrMo16 [39]									
Element	C	Si	Mn	P	S	Cr	Mo	Ni	Fe
% Weight	0.37	0.38	0.39	0.012	0.003	1.72	0.3	3.83	93

The contact configuration consists of a crossed flat-on-flat contact (Fig. 5a) tested on a hydraulic fretting wear experimental set-up (Fig. 5b) which is highly adapted to examine large horizontal crossed flat configurations. More detailed description of the test setup is provided elsewhere [14,37]. The fretted surface is rectangular in shape exhibiting a nominal contact area "$A = L_x.L_y$".

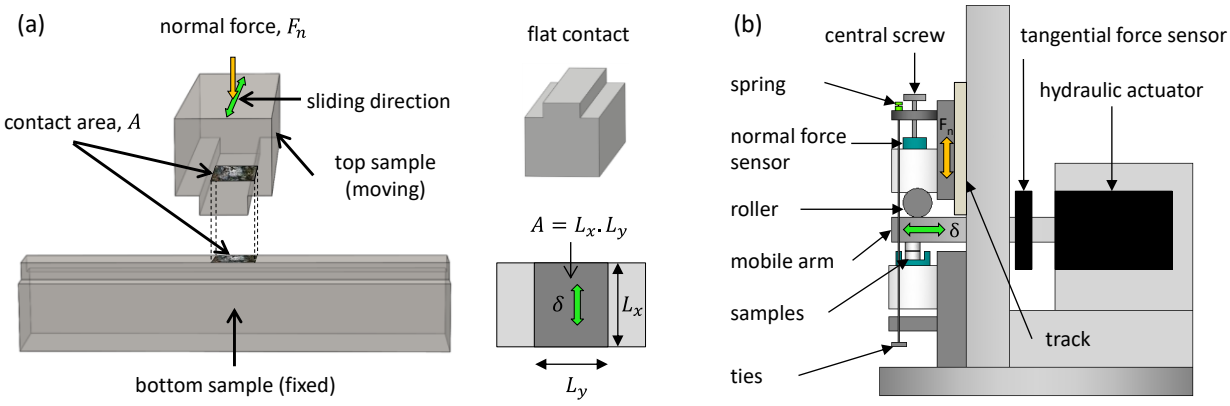

Fig. 5. Schematic diagrams showing the (a) crossed homogeneous flat-on-flat contact configuration and the (b) hydraulic fretting wear test system at LTDS (Laboratory of Tribology and Systems Dynamics).

Tests were conducted at ambient conditions of temperature (25 °C ± 5 °C) and humidity (RH=40% ± 10%). A major interest of this flat-on-flat interface compared to the usual Hertzian configuration is the possibility to keep constant the apparent contact area whatever the surface wear extension. Besides, former FEM surface wear simulations suggest that the contact pressure profile converges to a flat mean contact pressure distribution after few hundred cycles allowing a direct correlation with the given ADR model [37]. Three frequencies (f=0.5, 1, & 10 Hz) are investigated to calibrate the model while keeping constant the fretting cycles N=20000 cycles, contact pressure p=100 MPa, sliding amplitude δ_g=±100 µm, and the apparent contact area A=25 mm². Note that the number of fretting cycles was fixed at 20000 cycles to achieve the steady state friction regime which is reached after 5000 fretting cycles [37]. Former investigations [14] confirmed insignificant changes regarding the partition between abrasive and adhesive wear areas between 5000 to 40000 cycles. However, very long test conditions could eventually modify the dioxygen diffusion rate within the interface due to the progressive

surface wear which can therefore change the distribution between abrasive and adhesive wear domains. Unfortunately, this is not investigated in the current study and it will be addressed in future work.

The oxygen distance parameter "d_O" is defined experimentally using crossed EDX line scans (Fig. 6) (as detailed in [14]) and is computed as follows:

$$d_{O,X} = \frac{1}{2}.\left(d_{O,X_1} + d_{O,X_2}\right) \quad (38)$$

$$d_{O,Y} = \frac{1}{2}.\left(d_{O,Y_1} + d_{O,Y_2}\right) \quad (39)$$

$$d_O = \frac{1}{2}.\left(d_{O,X} + d_{O,Y}\right) \quad (40)$$

The adhesion area A_{ad} can be calculated from the area of the internal zone where the oxygen intensity is relatively low:

$$A_{ad} = d_{ad,X}\,.\,d_{ad,Y} \quad (41)$$

The abrasion area A_{ab} is inferred from the measured adhesion area A_{ad} and the total apparent contact area A such that:

$$A_{ab} = A - A_{ad} \quad (42)$$

The relative proportions of abrasion and adhesion areas are respectively given by:

$$\%A_{ab} = \frac{A_{ab}}{A} \quad (43)$$

$$\%A_{ad} = \frac{A_{ad}}{A} \quad (44)$$

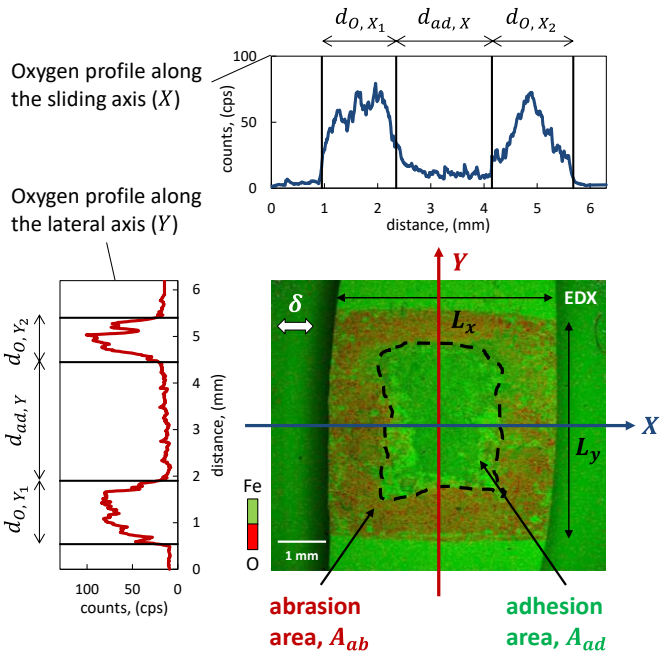

Fig. 6. Application of crossed EDX oxygen line scans method to estimate the oxygen distance "d_O" and the adhesion and abrasion areas (N=20000 cycles, p=100 MPa, δ_g=±100 µm, f=10 Hz and A=25 mm²) [14].

4.2 Properties of the debris layer porous medium

4.2.1 Longitudinal dispersivity (α_L)

The longitudinal dispersivity can be estimated from the contact sizes L_x and L_y following Pickens and Grisak relationship [34] such that:

$$\alpha_{L,x} = \frac{L_x}{10} \tag{45}$$

$$\alpha_{L,y} = \frac{L_y}{10} \tag{46}$$

4.2.2 Particle size (d_p)

Particle size can be obtained from the SEM-BSE analysis of the wear scar of the fretting tests and is found to have an average value around d_p=1 μm (Fig. 7). Former studies showed that the ejected debris is heterogeneous in nature consisting of loose and fine particles where only some plate-like fragments are occasionally present [40]. Shima and co-workers [41] revealed, through extensive investigation of particle size and morphology, that most of oxidized debris particles formed between steel surfaces have a diameter below 1 μm in addition to the presence of some oxide-coated large platelets. However, several studies demonstrated that debris particles formed in steel alloys have a size ranging from 0.01 to 1 μm [17,42–46] and some others reported a size ranging from 1 to 10 μm [47,48]. By combining the current SEM observations (Fig. 7) with the aforesaid literature investigations, it can be proposed that d_p=1 μm is appropriate assumption in the ADR model which will be backed by sensitivity analysis of particle size ranging from d_p=0.01 to 10 μm in the following discussion (Section 6).

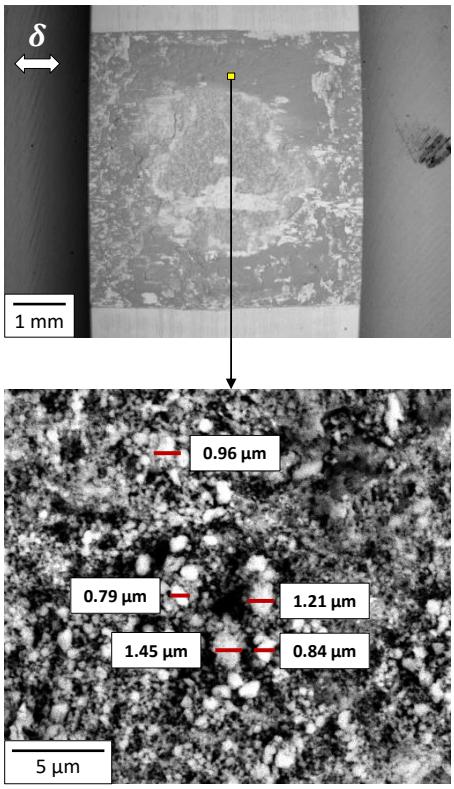

Fig. 7. SEM-BSE images showing the size of the particles constituting the debris bed after a fretting test (N=20000 cycles, p=100 MPa, δ_g=±100 µm, f=5 Hz and A=25 mm²).

4.2.3 Porosity of the debris bed (a)

One of the most challenging parameters in the ADR model is the estimation of the porosity parameter "a" of the debris layer related to a fretting wear interface. In fact porosity is influenced by many factors including particles' size, shape, and distribution [49,50], in addition to the contact pressure and contact configuration. However, in the current study due to the lack of information about the aforesaid parameters, porosity is computed by assuming that the debris bed is made up of spherical particles of identical size, packed in a cubic manner [51] (Fig. 8).

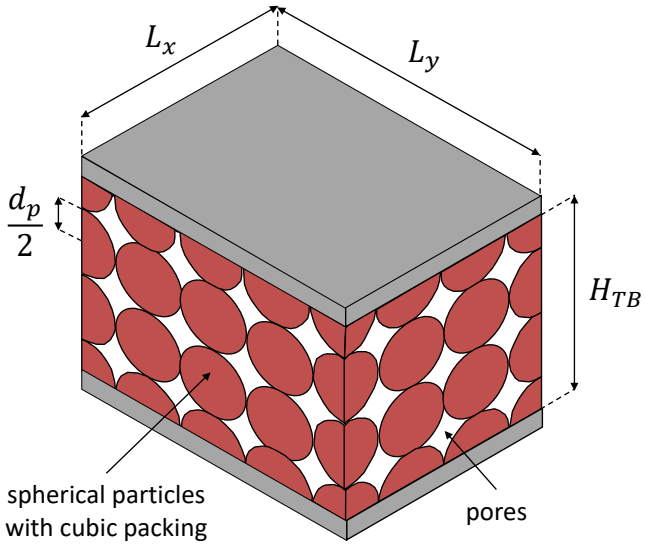

Fig. 8. Porosity estimation by assuming cubic packing of identical spheres in the debris bed.

Using these hypotheses, porosity can be approximated assuming a debris bed "bulk volume" (Fig. 8) such that $V_{bulk} = L_x.L_y.H_{TB}$ where the number of spheres constituting the debris bed is given by:

$$n = (L_x/d_p).(L_y/d_p).(H_{TB}/d_p) \tag{47}$$

Where H_{TB} is the thickness of the third body (debris bed). Thus the total volume of the matrix of solid particles is equal to the number of spheres (n) multiplied by the volume of one sphere:

$$V_{solid\ matrix} = n.\left(\frac{\pi}{6}.{d_p}^3\right) = \frac{\pi}{6}\left(L_x.L_y.H_{TB}\right) = \frac{\pi}{6}V_{bulk} \tag{48}$$

Consequently, the porosity of the debris bed is estimated by:

$$a = \frac{V_{pores}}{V_{bulk}} = \frac{V_{bulk} - V_{solid\ matrix}}{V_{bulk}} = 1 - \frac{\pi}{6} = 0.48 \tag{49}$$

This approximation of the porosity parameter "a", leading to a constant a=0.48 value, is based on a rough geometrical description of the debris layer which does not consider any loading parameter as the contact pressure for instance. Changing the contact pressure highly affects the debris bed porosity which influences in turn the permeability and consequently gas diffusion and oxygen distance. Hence, the effect of the contact pressure on powder porosity should be carefully addressed. Critical sate soil mechanics (CSSM) and powder metallurgy (PM) have provided many models relating pressure to porosity like Cam-Clay model [52] which is usually applied to model powder compaction [53] (Eq. 50).

$$a = \frac{a_0 - \lambda.(1-a_0).\mathrm{Log}\left(\frac{p}{p_0}\right)}{1 - \lambda.(1-a_0).\mathrm{Log}\left(\frac{p}{p_0}\right)} \tag{50}$$

With p_0 being the yield pressure of the particles (Pa), a_0 the initial porosity at p_0, and λ being the loading slope of the yield surface (Pa^{-1}) by neglecting the initial stage of elastic deformation of grains.

This more complete description requires the identification of "λ" variable which unfortunately cannot be addressed in the frame of this investigation. Therefore, and as a first approximation, the porosity variable "a" is set at 0.48.

4.2.4 Intrinsic permeability of debris layer (k)

The intrinsic permeability can be found through Carman-Kozeny equation (Eq. 8) [23,24] by using the particle size (d_p) and the porosity (a) values defined in the previous sections. Doing so, the intrinsic permeability of debris bed is found to be equal to k=2.27x10^{-15} m².

4.3 Threshold partial pressure ($P_{O_2,th}$)

Based on thermodynamic considerations, an oxide is produced on a metal surface whenever the oxygen potential in the environment is higher than the oxygen partial pressure in equilibrium with the oxide [54]. Below this equilibrium oxygen pressure, which is also referred to as oxide dissociation pressure, metal oxidation is not likely to take place. Iwabuchi and co-workers [55] showed that oxidative wear of an iron-based alloy is significant when oxygen partial pressure is above $P_{O_2,th}$=0.1 Pa where magnetite and hematite are detected, and adhesive transfer of metallic debris prevails below 0.1 Pa. They obtained these results by conducting gross slip fretting tests of S45C steel under oxygen-controlled environments at room temperature (23 °C ± 5 °C).

The studied low alloyed steel displays a quite similar composition as S45C. So, an equivalent $P_{O_2,th}$ can be considered.

Besides, the micro-Raman analysis of the external abrasive corona (Fig. 9), like the former Iwabuchi investigations, shows that the external oxide debris layer consists mainly of magnetite and hematite which again supports the chosen $P_{O_2,th}$ threshold value.

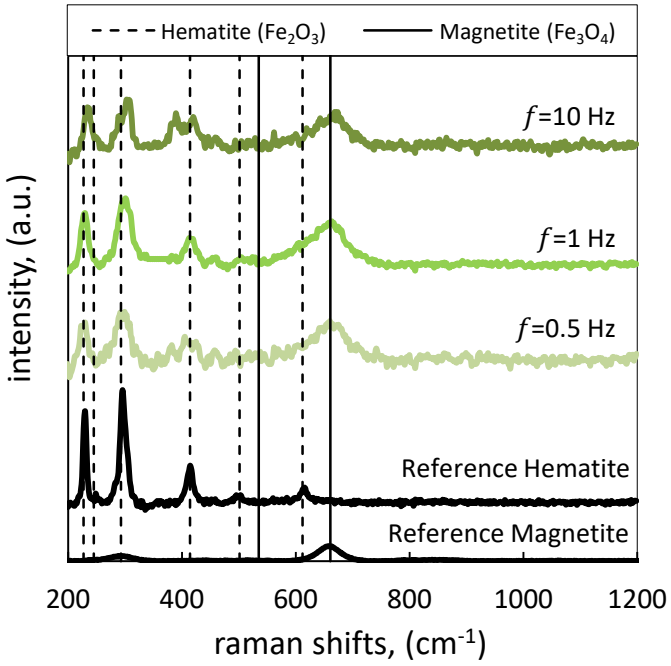

Fig. 9. Raman spectra of the oxide debris layer (external abrasive corona) related to the calibration tests (Table 3): f=0.5, 1 and 10 Hz (N=20000 cycles, p=100 MPa, δ_g=±100 µm and A=25 mm², for λ=785 nm, Laser power=0.35 mV, and acquisition time=150 s).

4.4 Identification of the reaction rate coefficient (r_{O_2})

Former investigations confirm that increasing the frequency and contact pressure tend to decrease the oxygen distance d_O [14]. Indeed, a higher friction power input in the fretted interface increases the reaction rate coefficient r_{O_2} between the fresh metal and the available dioxygen molecules which decreases in turn the oxygen partial pressure extending the inner adhesive wear domain and consequently decreasing the lateral d_O length scale. As mentioned previously, the reaction rate may depend on material properties as well as the contact loading parameters. Wear rate is usually formalized through the Archard theory expressing the wear volume extension as a function of the

accumulated Archard factor ΣW (N.m) defined as the product of the normal force multiplied by the sliding distance [56]. This wear process description is indirectly supported by the Bowden and Tabor theory suggesting that surface degradations occur through local interactions between rough surfaces where plastic deformations of contacting high spots (asperities) occurred [57]. They demonstrated that the real area of contact is proportional to the normal loading divided by the metal hardness which indirectly justifies that the wear rate is also proportional to the normal load. The local Archard's density parameter "w" (N.m/mm²) was successively considered to predict the wear depth extension whereas the related Archard's power density factor "ω" (N.m/mm²/s), also related to the so-called "pv" factor, is commonly adopted to describe metal seizure phenomena. This latter variable is very interesting as it describes the local friction work rate inputted within the interface to damage the surfaces. In a first approximation, the reaction rate coefficient monitoring the di-oxygen reaction is therefore expressed as a function of the Archard power density factor ω (N.m/mm²/s or W/mm²) given for the studied fretting sliding condition:

$$\omega = p \times \mathrm{v} = \left(\frac{F_n}{A}\right) \times \left(4.\delta_g.f\right) = 4.p.\delta_g.f \tag{51}$$

Former experimental investigations [14] underlined a power-law decreasing evolution of the oxygen distance d_O with the increase in the sliding frequency and the contact pressure. So, as a first approximation, the sink term "r_{O_2}" is assumed, by heredity, to have a power-law growth with the Archard power density factor such that:

$$r_{O_2} = \beta \left(\frac{\omega}{\omega_{ref}}\right)^{\gamma} \tag{52}$$

ω_{ref} is the Archard power density factor at the reference conditions (N=20000 cycles, p=100 MPa, F_n=2500 N, δ_g=±100 μm, f=1 Hz, L_x=L_y=5 mm, and A=25 mm²) so that ω_{ref}=0.04 W/mm². β and γ coefficients can be calculated by simulating only three calibration tests varying the frequency at f=0.5, 1 and 10 Hz but keeping constant the other parameters (N=20000 cycles, p=100 MPa, F_n=2500 N, δ_g=±100 μm, L_x=L_y=5 mm, and A=25 mm²). Both β and γ are tuned in order to minimize the error between the experimental d_O values ($d_{O,exp}$) measured in the fretting scars and the predictions given by the ADR approach ($d_{O,ADR}$) assuming the former hypotheses for the other variables of the model. The best fitting is achieved with β=394.63 and γ=0.47 (Table 3).

Table 3. Calibration of the reaction rate coefficient (r_{O_2}) (Eq. 51) (β=394.63 and γ=0.47) for 34NiCrMo16 interface with N=20000 cycles, p=100 MPa, δ_g=±100 μm and A=25 mm².

Frequency, f (Hz)	Archard power density factor, ω (W/mm²)	Experimental oxygen distance, $d_{O,exp}$ (mm)	Numerical oxygen distance, $d_{O,ADR}$ (mm)	Relative error, (%)
0.5	0.02	2.3	2	13
1	0.04	1.5	1.7	13
10	0.4	1.1	1.1	0

4.5 Qualitative comparison with fretting experiments

Fig. 10a and b compare the evolution of the steady state total pressure (P) and oxygen gas partial pressure (P_{O_2}). Although the dioxygen partial pressure drastically decreases from 21278.2 Pa to 3.06x10^{-9} Pa at the center of the contact, the total pressure displays a small diminution of about 10%. This tendency is explained by the fact that nitrogen gas

compensates the elimination of oxygen gas inducing a 10% increase in N_2 partial pressure in the inner part of the interface. This pressure balance is driven by the advection process of the entire gas mixture (i.e. bulk flow) activated by the total pressure gradients. The target of the model, which is to predict the adhesive versus abrasive wear extension, is illustrated in Fig. 10c and d where the 2D EDX map of the fretting scar is compared to the 2D simulation of the dioxygen partial pressure in the fretted interface. By considering $P_{O_2,th}$=0.1 Pa, the limit between the adhesion and abrasion zones can be established. A very good correlation is observed with the experiments where pure metal interactions are observed in the inner part of the fretting scar (green=very poor oxygen concentration) whereas abrasive-oxidational processes are occurring in the d_O width corona (brick red=high oxygen concentration).

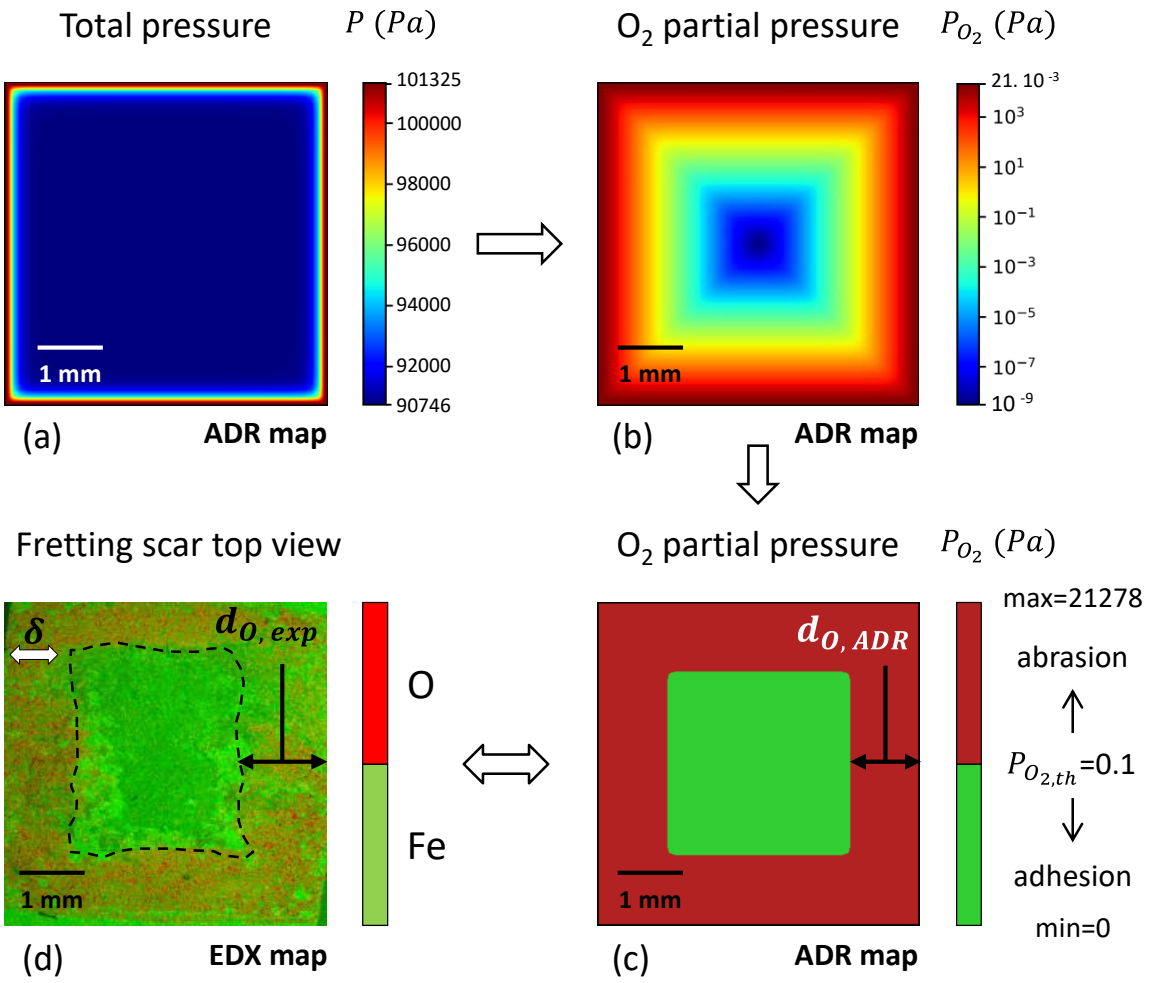

Fig. 10. Comparison between the 2D simulation of the dioxygen partial pressure at steady the steady state ($r_{O_2} = \beta\left(\frac{\omega}{\omega_{ref}}\right)^{\gamma}$ with β=394.63 and γ=0.47, ω_{ref}=0.04 W/mm², $P_{O_{2,th}}$=0.1 Pa, a=0.48, d_p=1 µm, k=2.27x10^{-15} m², and $\alpha_{L,x}$=$\alpha_{L,y}$=0.0005 m) and EDX mapping of the studied fretting scar (34NiCrMo16 / 34NiCrMo16 , N=20000 cycles, p=100 MPa, δ_g=±100 µm, f=10 Hz and A=25 mm²) with: (a) ADR map showing the evolution of the total pressure; (b) ADR map showing the evolution of dioxygen partial pressure (log scale); (c) ADR map representing the partition between abrasion and adhesion; (d) EDX map showing the fretting scar top view.

This multiphysics ADR model of the adhesive/abrasive wear extension in fretting appears as a real opportunity to predict fretting processes. Based on a physical description of wear and dioxygen diffusion processes within the debris layer, ADR requires a limited number of variables and can be calibrated using a limited number of fretting experiments. However, to validate this approach, the given model will be compared versus various sliding frequencies, contact pressures and contact sizes.

5. Model validation

5.1.1 Test strategy

To check the validity of ADR model, former experimental results (detailed in [14]) outside the current calibration conditions are simulated. The main results of this experimental work are presently recalled. A reference test (repeated three times) having a number of cycles N=20000 cycles, contact pressure p=100 MPa, sliding amplitude δ_g= ±100 µm, frequency f=1 Hz, and a square contact area A=25 mm² (L_x=L_y=5 mm) is considered (Fig. 11). Following this, a cross-experimental scheme is performed such that the sliding frequency “f” is examined from 0.5 to 10 Hz, the contact pressure “p” from 25 to 175 MPa and the apparent contact area “A” is varied from 10 to 25 mm².

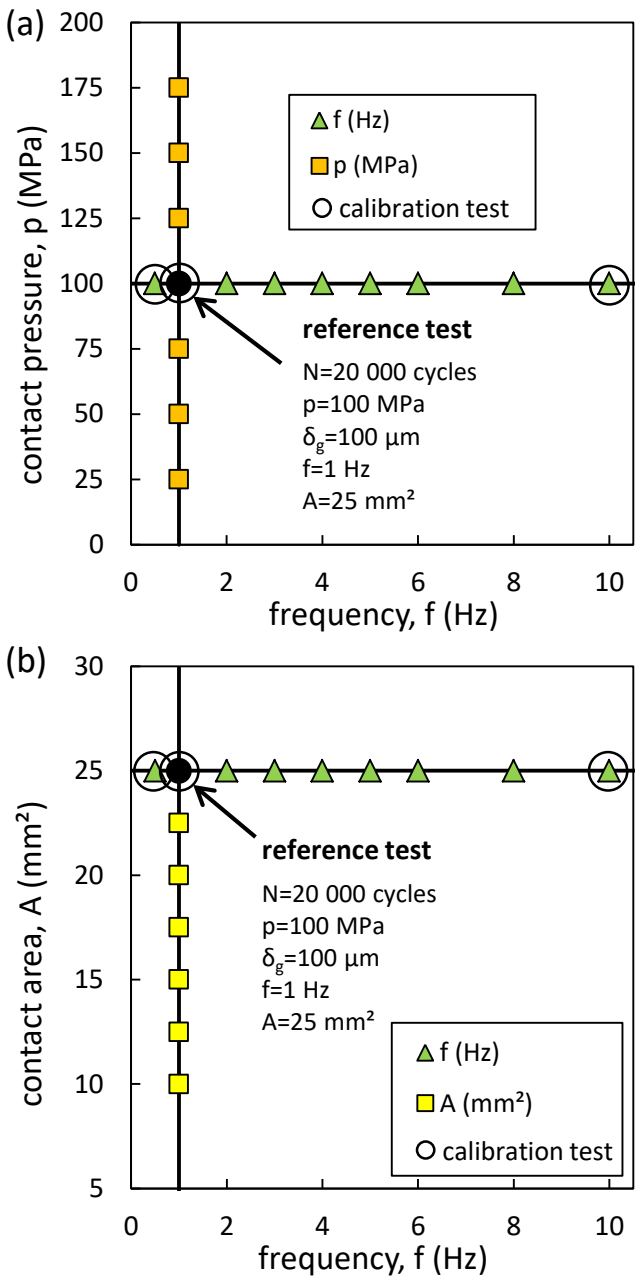

Fig. 11. Cross-experimental strategy to validate the ADR approach for plain crossed flat-on-flat samples: (a) contact pressure versus frequency; and (b) apparent contact area versus frequency.

5.1.2 Variable sliding frequency (f)

Fig. 12 displays the evolution of dioxygen partial pressure profile along the median axes L_x and L_y as a function of the applied frequency from 0.5 to 10 Hz. As previously mentioned, increasing frequency leads to growth of the inner zone where $P_{O_2} < P_{O_2,th}$ resulting in expansion of the adhesion area and consequently lower oxygen distance. This is due to the fact that for higher frequencies the metal exposure rate and therefore the rate of oxidation reaction with the existing interfacial dioxygen molecules are increased [9]. Hence, a high oxygen consumption rate at the borders limits oxygen gas availability towards the center of the contact.

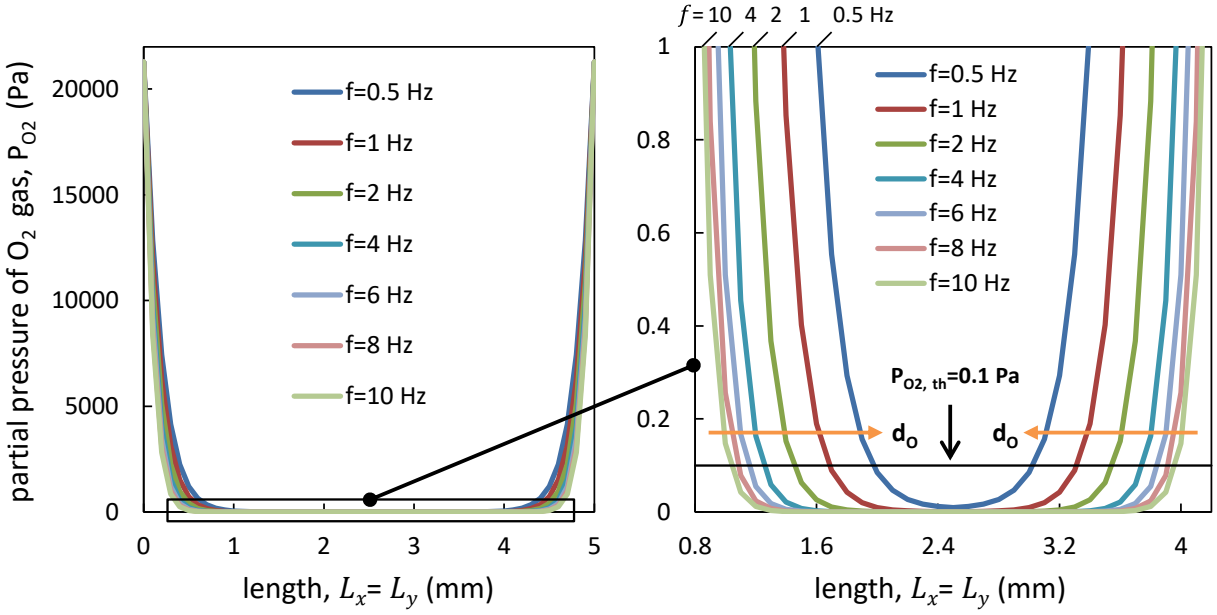

Fig. 12. Evolution of oxygen partial pressure with the increase in frequency from 0.5 to 10 Hz (N=20000 cycles, p=100 MPa, δ_g=±100 µm, and A=5x5=25 mm²).

Fig. 13 shows the evolution of the EDX maps and line scans with the increase in frequency compared with those predicted numerically by ADR approach. Note that numerical line scans are constructed by giving two arbitrary high and low constant intensities for $P_{O_2} > P_{O_2,th}$ and $P_{O_2} < P_{O_2,th}$ respectively. A rather good correlation is observed between numerical ADR simulations and experimental results. Indeed, both of them show extension of the inner adhesion area with the increase of the frequency from 0.5 to 10 Hz. It is worth mentioning that the latter exhibits an evident square shape (especially at 10 Hz) which is also captured by the simulations validating the hypothesis of oxygen distance isotropic distribution in case of square contact area.

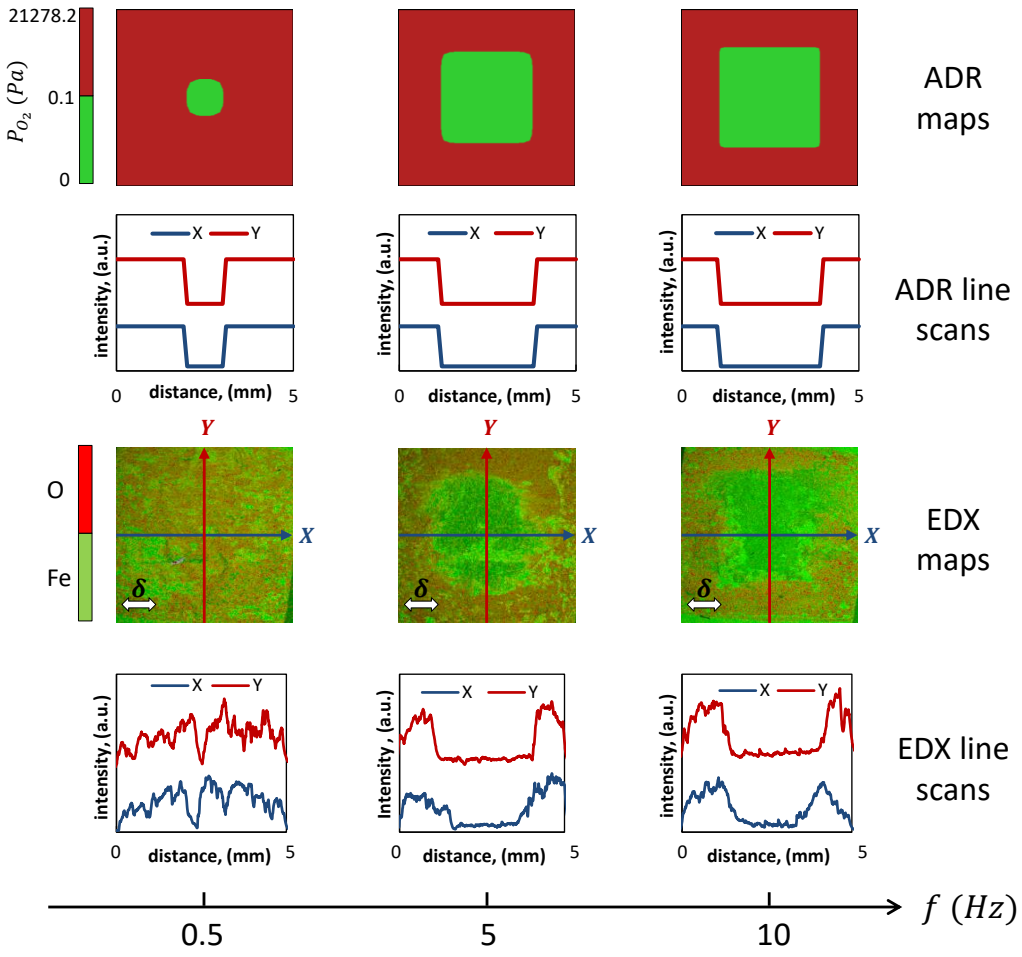

Fig. 13. Correlation between EDX and numerical ADR maps and the corresponding line scans revealing the growth of adhesion zone with the increase in the sliding frequency from 0.5 to 10 Hz (N=20000 cycles, p=100 MPa, δ_g=±100 µm, and A=5x5=25 mm²).

Fig. 14 compares the evolution of the experimental and numerical oxygen distance values d_O defined from Eq. 40 for frequencies ranging from 0.5 to 10 Hz. Established from only three calibration tests (f=0.5, 1 & 10 Hz), this analysis confirms that the ADR approach is able to capture the decreasing trend of the oxygen distance obtained experimentally with a correlation coefficient reaching 99%.

From the ADR simulation, a simplified power law can be extracted such that:

$$d_O = 1.72 \times f^{-0.21} \tag{53}$$

This result is very interesting as it shows that using the ADR physical modelling of the COC, it is possible to demonstrate the empirical power law formulation previously introduced in [14] to formalize the evolution of d_O as a function of the applied frequency.

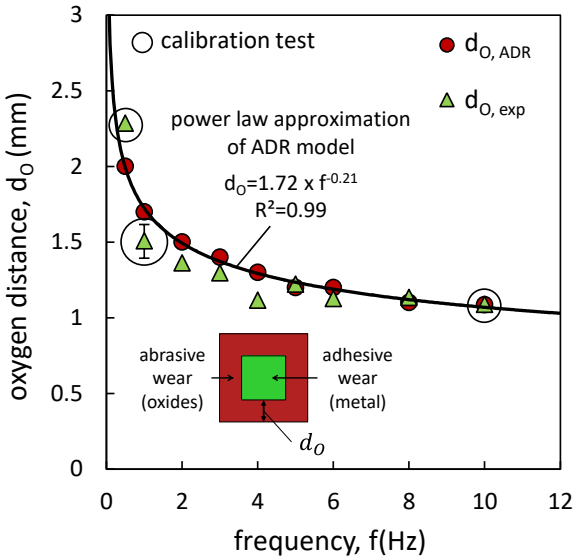

Fig. 14. Correlation between the experimental ($d_{O,exp}$) and the predicted oxygen distance from ADR approach ($d_{O,ADR}$) as a function of the sliding frequency (N=20000 cycles, p=100 MPa, δ_g=±100 µm, and A=5x5=25 mm²).

5.1.3 Variable contact pressure (p)

Fig. 15 displays the evolution of the dioxygen partial pressure profile along the median axes L_x and L_y with respect to the contact pressure varying from 25 to 175 MPa. As the case of frequency, increasing the contact pressure induces an increase in the Archard power density factor triggering in turn a higher consumption of the dioxygen molecules.

This restrains the oxygen gas availability towards the center of the interface shifting the contact from pure abrasive to mixed abrasive-adhesive wear.

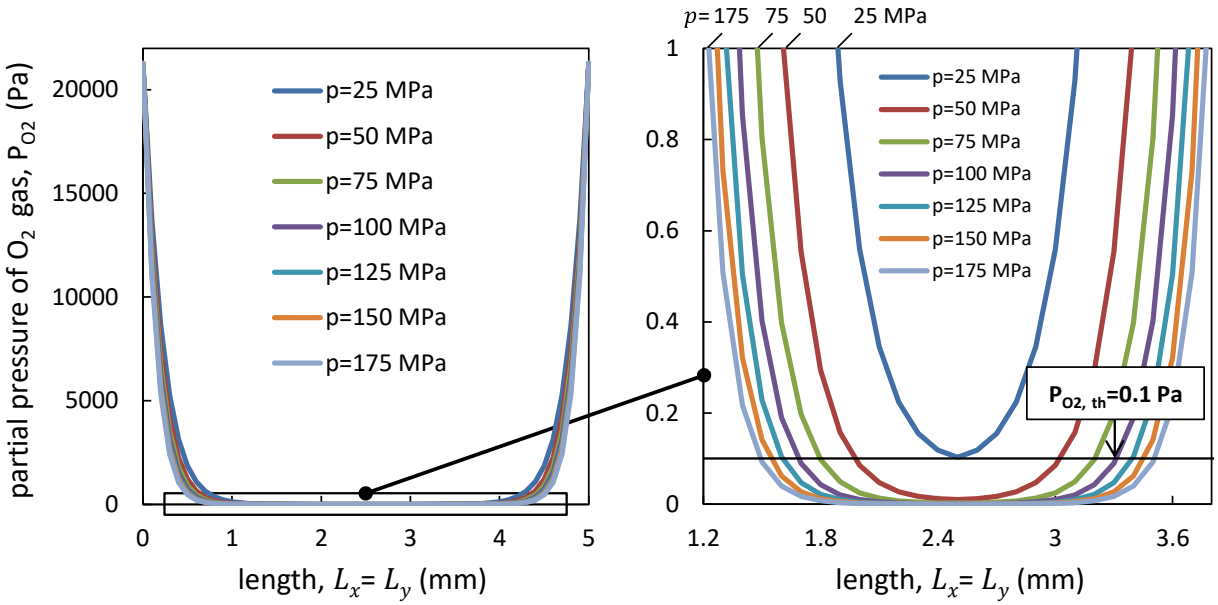

Fig. 15. Evolution of oxygen partial pressure with the increase in contact pressure from 25 to 175 MPa (N=20000 cycles, f=1 Hz, δ_g=±100 µm, and A=5x5=25 mm²).

EDX maps and line scans are compared with those predicted numerically by ADR approach at different contact pressures (Fig. 16). The experimental and numerical results appear to be highly correlated as both of them clearly reflect the remarkable shift in the wear regime from pure abrasive wear at low pressure (p=25 MPa) to a mixed abrasive-adhesive wear when higher Archard power is dissipated in the interface.

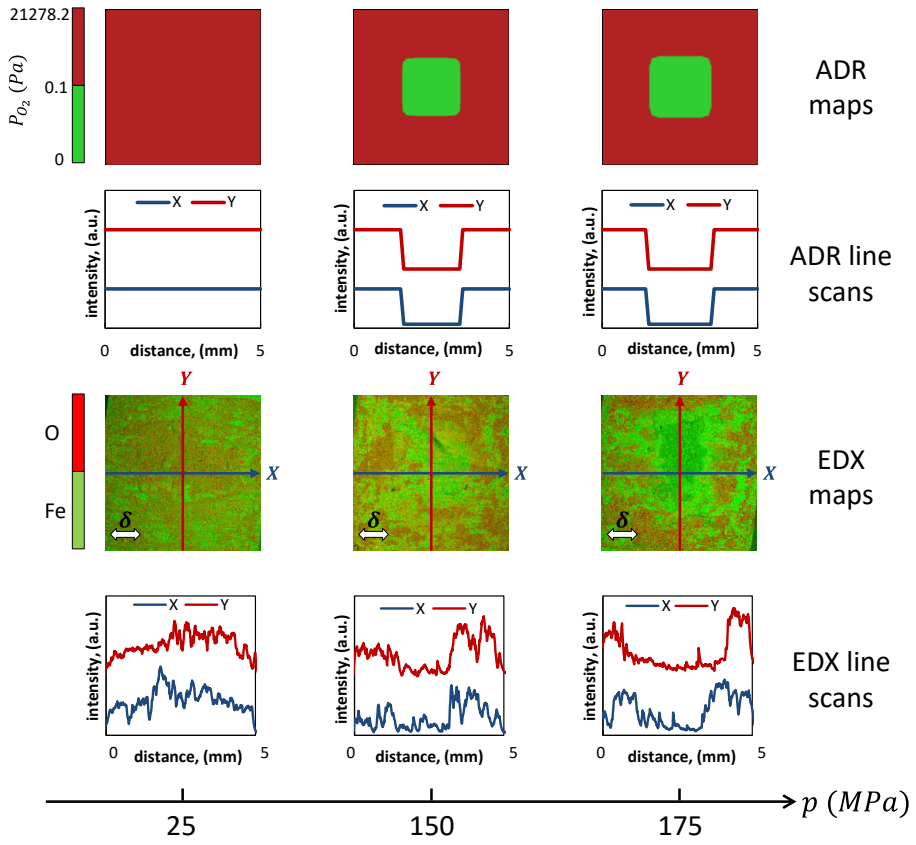

Fig. 16. Correlation between EDX and numerical ADR maps and the corresponding line scans showing the growth of adhesion zone with the increase in the contact pressure from 25 to 175 MPa (N=20000 cycles, f=1 Hz, δ_g=±100 µm, and A=5x5=25 mm²).

Fig. 17 displays the evolution of the experimental and numerical oxygen distance values d_O (Eq. 40) for contact pressures ranging from 25 to 175 MPa. The decreasing evolution of d_O is markedly detected by the ADR model where a simplified power law can be estimated such that:

$$d_O = 5.34 \times p^{-0.24} \tag{54}$$

A very good correlation is observed between the model and the experiments although no pressure calibration was done. This indirectly supports the stability of the model and

the Archard power density factor as a pertinent variable to formalize the reaction rate of the di-oxygen molecules. The ADR model slightly overestimates the oxygen distance observed experimentally. This comes from the fact that increasing the contact pressure compacts the surface roughness and the debris layer which reduces the porosity and hence the permeability of the latter. Therefore, the diffusion of dioxygen molecules towards the center of the interface will be very limited [14]. However, in the current investigation and for the sake of simplicity, the porosity is assumed to be constant (a=0.48) whatever the loading condition. This fact can explain the slight discrepancy recognized between experimental and numerical ADR results. Undeniably, by introducing a dynamic porosity dependent on contact pressure (Eq. 50), this difference can be easily reduced. Unfortunately due to the lack of experimental data the effect of contact pressure on porosity cannot be formalized.

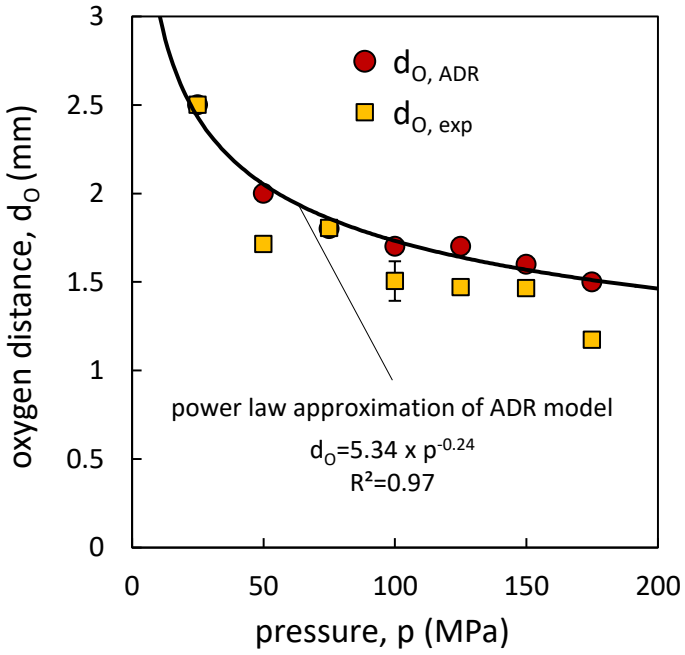

Fig. 17. Correlation between the experimental ($d_{O,exp}$) and the predicted oxygen distance from ADR approach ($d_{O,ADR}$) as a function of the contact pressure from 25 to 175 MPa (N=20000 cycles, f=1 Hz, δ_g=±100 µm, and A=5x5=25 mm²).

5.1.4 Archard power density factor formulation

Fig. 18 compiles the evolution of the experimental and numerical oxygen distance as a function of the Archard power density factor (i.e. “pv” factor) for various contact pressures and sliding frequencies. Interestingly, all data points appear to follow a single master curve which can be predicted by the ADR model as:

$$d_O = 0.87 \times \omega^{-0.22} \quad (55)$$

This very nice correlation involving a wide range of experiments confirms the stability of the model and comes in agreement with the contact oxygenation concept (COC) which suggests that the higher the Archard power density dissipated in the contact, the faster the consumption of di-oxygen molecules and consequently the smaller the oxygen distance. Similar tendency was observed in previous studies on titanium [9,10] and steel alloys [58]. The given results are established for the studied steel interface. Other “non-noble” metallic materials, exhibiting different surface reactivity with oxygen like copper, aluminum or titanium alloys, may lead to different results. Hence, further works will be done to evaluate how the proposed formulation can be applied to predict the partition between abrasive and adhesive wear areas in fretting interfaces (i.e. the oxygen distance) for various metal alloys and various loading conditions.

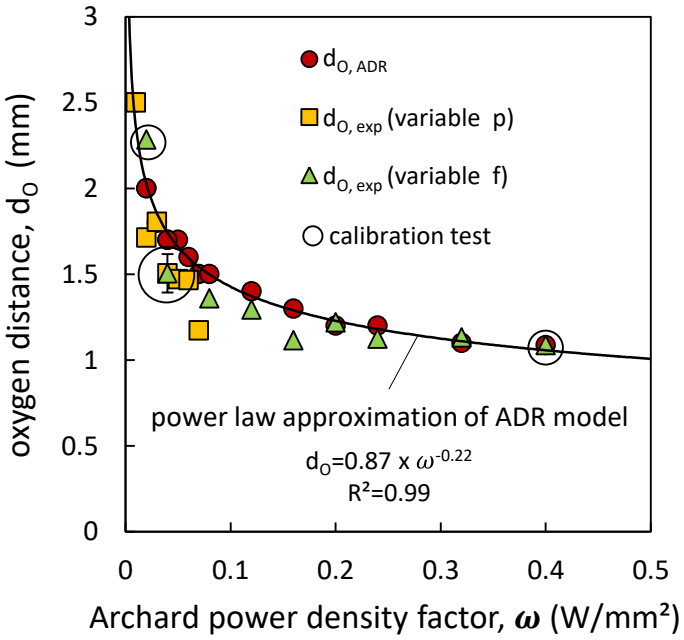

Fig. 18. Correlation between the experimental ($d_{O,exp}$) and the predicted oxygen distance from ADR approach ($d_{O,ADR}$) as a function of Archard power density factor ω (N=20000 cycles, δ_g=±100 µm, and A=5x5=25 mm²).

5.1.5 Variable contact area (A)

The evolution of oxygen partial pressure with the apparent contact area is depicted in Fig. 19. Indeed, assuming that contact size does not affect the dioxygen consumption rate, it is expected from COC to achieve homothetic oxygen partial pressure profiles. This tendency is effectively confirmed by the given ADR approach. For small contact area, P_{O_2} profile remains above $P_{O_2,th}$. On the other hand, P_{O_2} profile decreases below $P_{O_2,th}$ for larger contact areas since the latter is large enough to consume the available dioxygen molecules before reaching the center of the contact.

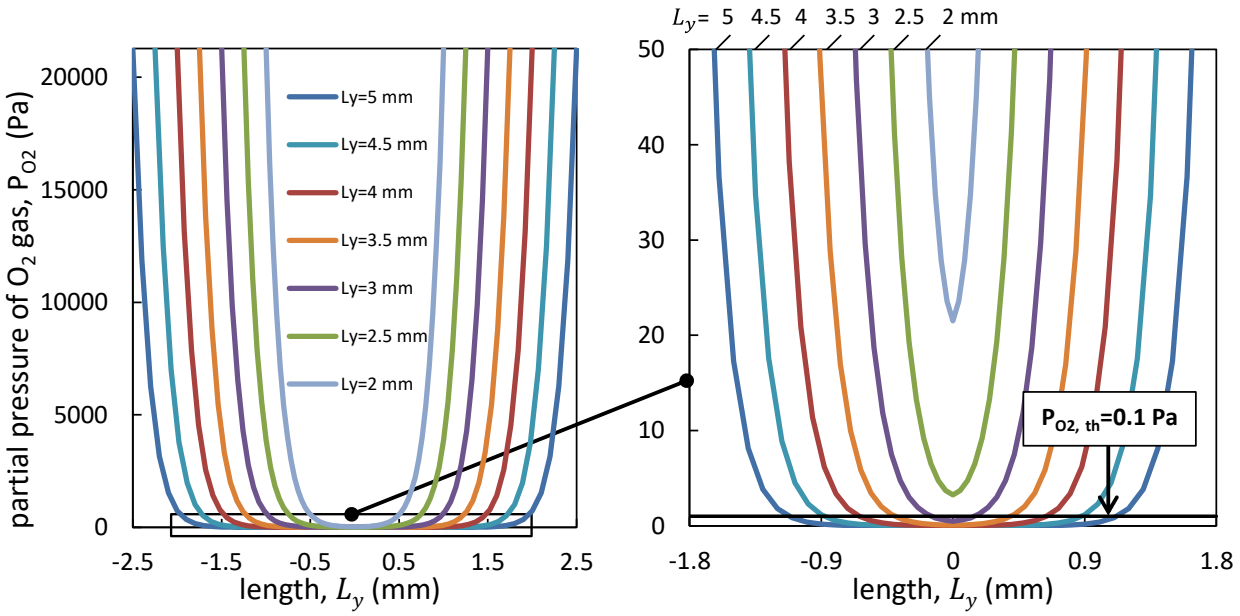

Fig. 19. Evolution of oxygen partial pressure with the increase in the apparent contact area from 10 to 25 mm² (N=20000 cycles, p=100 MPa, δ_g=±100 µm, and f=1 Hz).

Fig. 20 compares the evolution of the EDX maps and line scans to those predicted numerically by ADR approach at different contact areas. Once again, good correlation is observed between numerical and experimental results. As reflected experimentally by EDX analysis, decreasing the contact area causes a remarkable recession in the adhesive wear until it completely vanishes when the contact area is less than 15 mm². This tendency is predicted by the given ADR model where both numerical maps and line scans seem to highly mimic the experimental EDX observations.

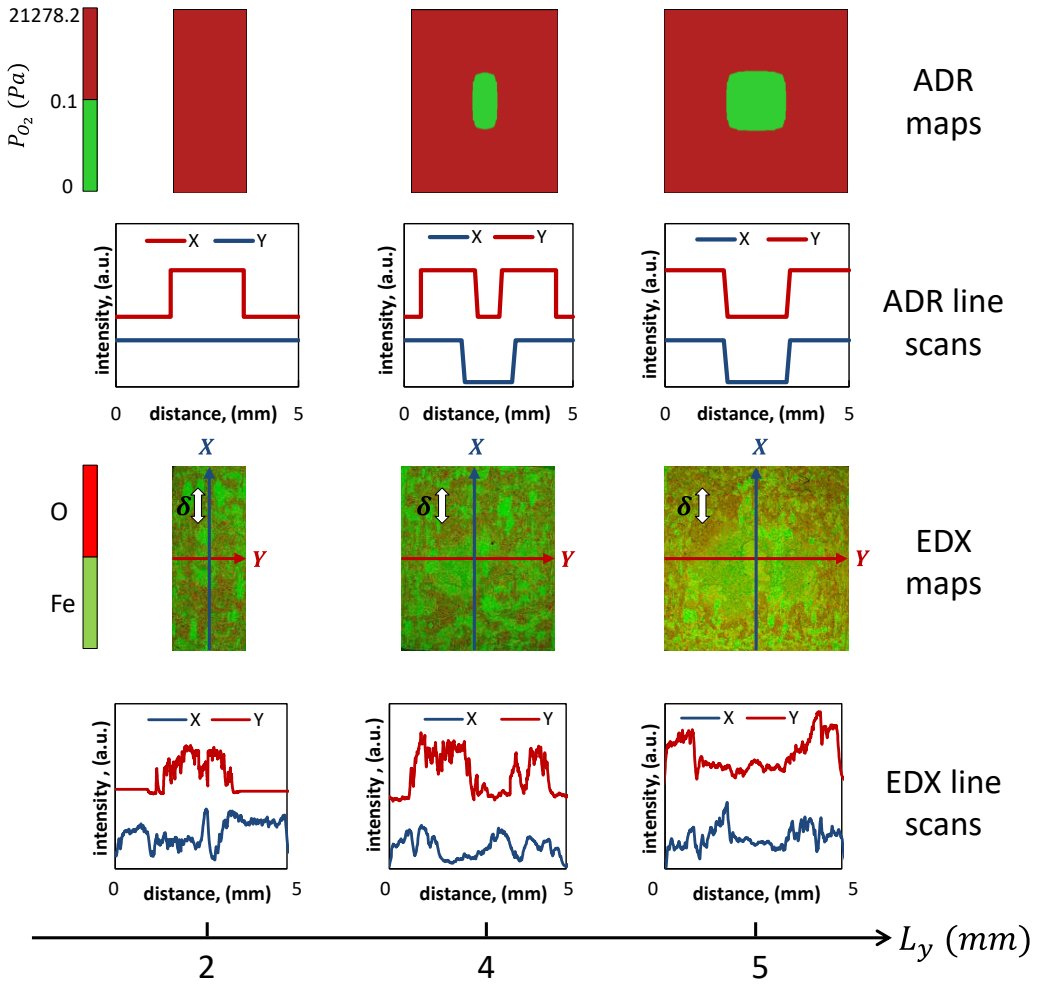

Fig. 20. Correlation between EDX and numerical ADR maps and the corresponding line scans showing the growth of adhesion area with the increase of the apparent contact area from 10 to 25 mm² (N=20000 cycles, p=100 MPa, δ_g=±100 µm, and f=1 Hz).

Fig. 21 illustrates the evolution of the experimental and numerical oxygen distance values d_O defined from Eq. 40 when variable contact area is investigated. Note that the data points are limited to the cases where the adhesion area is not zero (i.e. $A_{ad} > 0$). In fact, both experiments and simulation reveal the same tendency showing constant d_O around 1.60 mm whatever the contact size. However, ADR model seems to slightly overestimate the d_O oxygen distance which might be ascribed to a slight overestimation

of the porosity and/or the threshold oxygen partial pressure. Nevertheless, the mean relative error is nearly 16% which indirectly supports the stability of the proposal.

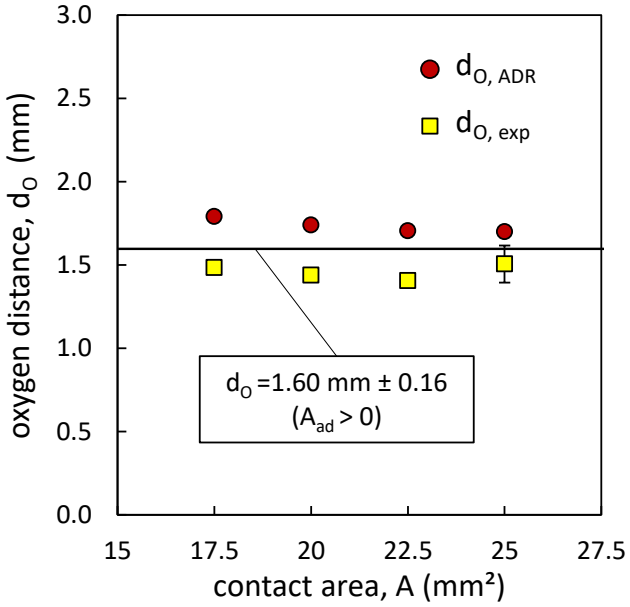

Fig. 21. Correlation between the experimental ($d_{O,exp}$) and the predicted oxygen distance from ADR approach ($d_{O,ADR}$) as a function of the apparent contact area for A_{ad}>0 (N=20000 cycles, p=100 MPa, δ_g=±100 µm, and f=1 Hz).

5.1.6 Quantitative validation of ADR approach

The experimental oxygen distance "$d_{O,exp}$" is compared with that expected by ADR approach "$d_{O,ADR}$" such that the data points associated to pure abrasive wear (i.e. A_{ad}=0) are excluded from the analysis. By combining the results of variable contact area, contact pressure and sliding frequency, a good correlation emerges as shown in Fig. 22a. This lends support to the current ADR approach as an effective tool to predict the oxygen distance at different loading conditions.

Fig. 22b compares the experimental abrasive wear area ($A_{ab,exp}$) to that foretold by ADR approach ($A_{ab,ADR}$) considering full abrasive and mixed abrasive-adhesive wear regimes. A very good correlation (R^2=0.99) unfolds between the experimental abrasion areas and those predicted by ADR model. The model was calibrated using only 3 frequency tests whereas Fig. 22 compiles more than 24 experiments varying frequency, contact pressure and contact size. This indirectly supports the stability of the given ADR approach to predict the partition of between abrasive and adhesive wear domains in fretting interfaces.

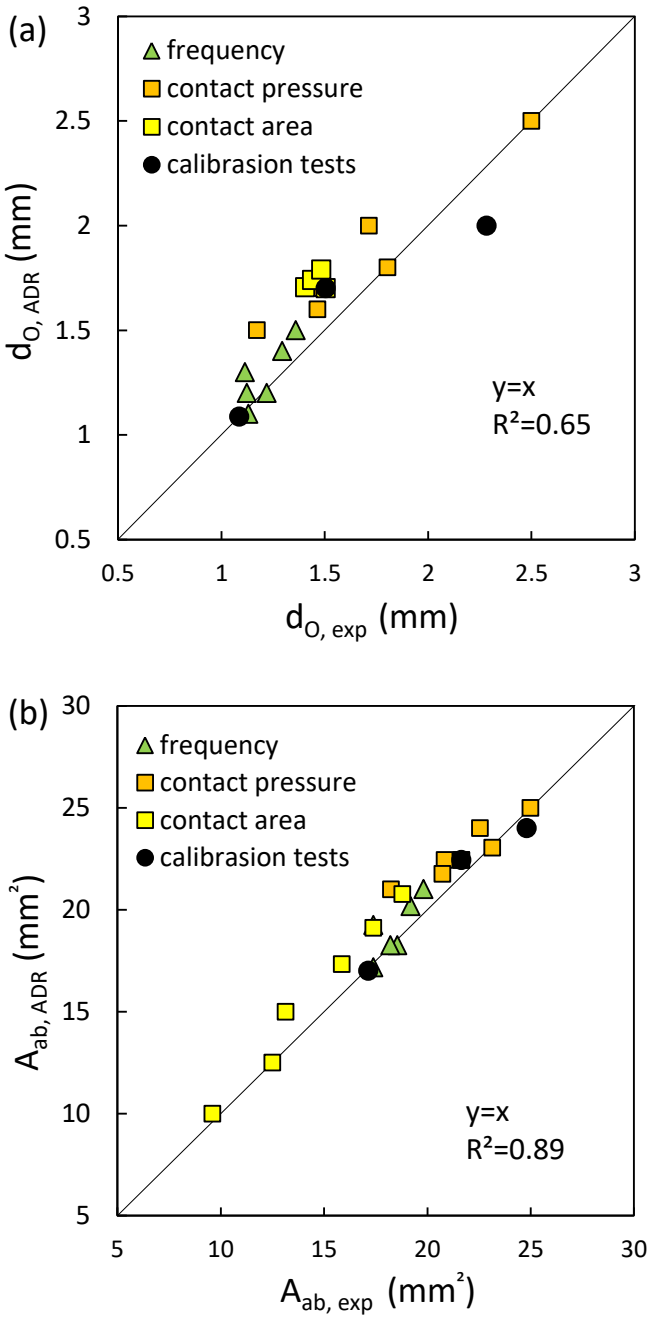

Fig. 22. Comparing the experimental and the predicted results (ADR approach) for (a) the oxygen distance "d_O"; and (b) the abrasion area "A_{ab}".

6. Discussion

The current study aims at explaining and modelling contact oxygenation process within a flat-on-flat fretting interface. An advection-dispersion-reaction approach (ADR) is suggested such that the debris bed is considered a compact powdery porous medium allowing the transport of atmospheric gases namely oxygen and nitrogen. The oxidation reaction of freshly exposed metal provides an important sink term for oxygen gas. This promotes a change of the gas consumption inducing pressure and concentration gradients within the contact which trigger advection and dispersion processes. By assuming that nitrogen gas has a negligible interaction with the exposed metal during fretting, the given ADR model permits capturing the decay of oxygen partial pressure from the borders towards the center of the contact which explains the contact oxygenation concept. Defining a threshold oxygen partial pressure $P_{O_2,th}$, the partition between abrasion-oxidation and adhesion domains can be predicted whereby oxidation prevails whenever $P_{O_2} \geq P_{O_2,th}$, and adhesion is activated otherwise. Based on this assumption, oxygen distance can be defined numerically as the distance between the contact borders and the position where oxygen pressure start to fall below $P_{O_2,th}$. This allows comparing experimental and numerical results by tracking oxygen distance value. Former studies showed that contact pressure and sliding frequency highly affect wear mechanisms [9,14]. Indeed, low loading conditions induce low Archard power density factor ω (i.e. equivalent “p.v” factor). This leads to pure abrasive wear over the whole interface. On the other hand, high Archard power density factor triggers composite adhesive-abrasive wear exhibiting metal transfers in the inner part of the contact enclosed by an abrasive wear corona on the lateral sides. This partition in wear

mechanisms stems from the raise in surface shear strain rate, metal exposure rate and ultimately the rate of the reaction with the interfacial dioxygen molecules. As a result, higher oxygen consumption and consequently smaller oxygen distance will be obtained. Viewed in this light, increasing the Archard power density factor is translated in the ADR approach by increasing the reaction term of dioxygen molecules. Doing so, oxygen distance along with abrasion-adhesion EDX maps can be simulated.

The model is further validated for wide range of sliding frequencies, contact pressures and contact sizes using plain crossed flat-on-flat samples. In fact, by decreasing the contact size, while keeping the same reaction rate, oxygen partial profiles will translate progressively from below to above $P_{O_2,th}$ which induces transition from mixed abrasive-adhesive to full abrasive domain.

Good predictions were achieved although many hypotheses have been considered to describe the interface. Thus, it appears interesting to evaluate how debris bed properties namely the porosity, particle size and permeability can influence these predictions. A sensitivity analysis was therefore carried out where these parameters are varied separately while fixing the tribological loadings on the reference condition (i.e. N=20000 cycles, p=100 MPa, δ_g=±100 µm, f=1 Hz, and A=25 mm²) (Fig. 23).

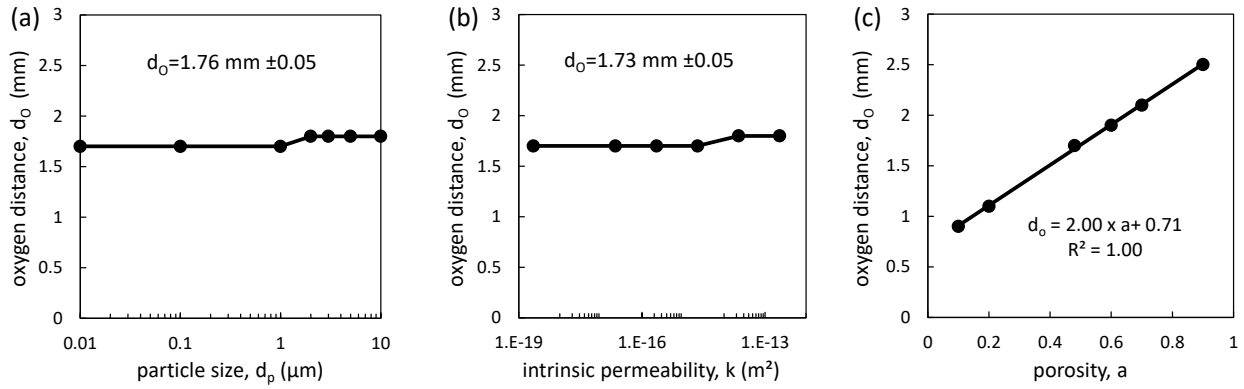

Fig. 23. Evolution of the oxygen distance d_O as a function of (a) the particle size "d_p", (b) the intrinsic permeability of the debris bed "k" and (c) the porosity "a" computed for the reference loading conditions (i.e. N=20000 cycles, p=100 MPa, δ_g=±100 µm, f=1 Hz, and A=25 mm²).

It appears that the particle size and the intrinsic permeability have little effect on the oxygen distance which remained unchanged around d_O≈1.7 mm. A variation of the particle size from 1 to 10 µm and a fluctuation of the permeability from 2.27x10^{-15} to 2.27x10^{-13} m² lead to a small increase of the contact oxygenation (i.e. oxygen distance d_O) of less than 5%. This smooth rising can be attributed to the easier access of oxygen provided by the higher particle size and consequently higher permeability based on Eq. 8. By contrast, the porosity of the debris bed plays a critical effect on the contact oxygenation. When this latter rose from 0.1 to 0.9, the oxygen distance increased linearly from 0.9 to 2.5 mm shifting the interface from severely adhesive to pure abrasive wear. This is due to the fact that increasing the porosity, likewise the particle size and permeability, allows more access of oxygen to the inner part of the surface and consequently higher oxygen distance. However, the little sensitivity of the model to the particle size and permeability compared to the case of porosity stems from the fact that

the former affect only advection process whereas the latter affects both advection and diffusion processes. This suggests also that the gas transport is much more governed by diffusion than by advection process which comes in agreement with previous studies reported in literature [18,33]. Note that when increasing the particle size, the porosity and the permeability beyond 5 µm, 0.8 and $5x10^{-14}$ m² respectively, the time step has to be decreased by 10 to 100 times which implies higher computation cost. To conclude, it can be argued that among the debris bed properties, the driving factor is the porosity coefficient. This suggests that future development must be undertaken to establish direct and/or indirect identification procedures to properly formalize this value, taking into account for instance the effect of the contact pressure or the sliding conditions. However, applying a basic estimation of this latter variable, this investigation proposes that ADR model coupled with COC concept appears as a pertinent quantitative starting approach not only to explain the partition between abrasive-oxidative and adhesive wear but also the transition in wear mechanisms from mixed abrasion-adhesion to full abrasion when several loading conditions are considered.

As previously mentioned, this analysis only considers the dioxygen molecules as driving parameters of the wear processes. However, the ADR model is also able to establish the partition between dioxygen and dinitrogen concentrations within the interface. Fig. 24a portrays the evolution of the partial pressures of oxygen and nitrogen gases along with the total pressure within the debris bed at the reference test in 2D and 3D. As expected by contact oxygenation concept, the partial pressure of O_2 gas is maximum at the borders of the contact. Then it decreases as the oxygen traverses the borders towards the center of the contact. On the other hand, the partial pressure of N_2 is

minimum at the borders (i.e. similar to ambient air condition) but increases inside the contact due to the advection process which tends to compensate the decay in the total pressure of the gas mixture. This conclusion is quite interesting as it suggests that in the inner part of the contact, an additional N_2 partial pressure is observed which can explain and potentially quantify the exotic nitriding process observed at room temperature in the inner part of titanium fretting interfaces (Fig. 24b) [9,10,35].

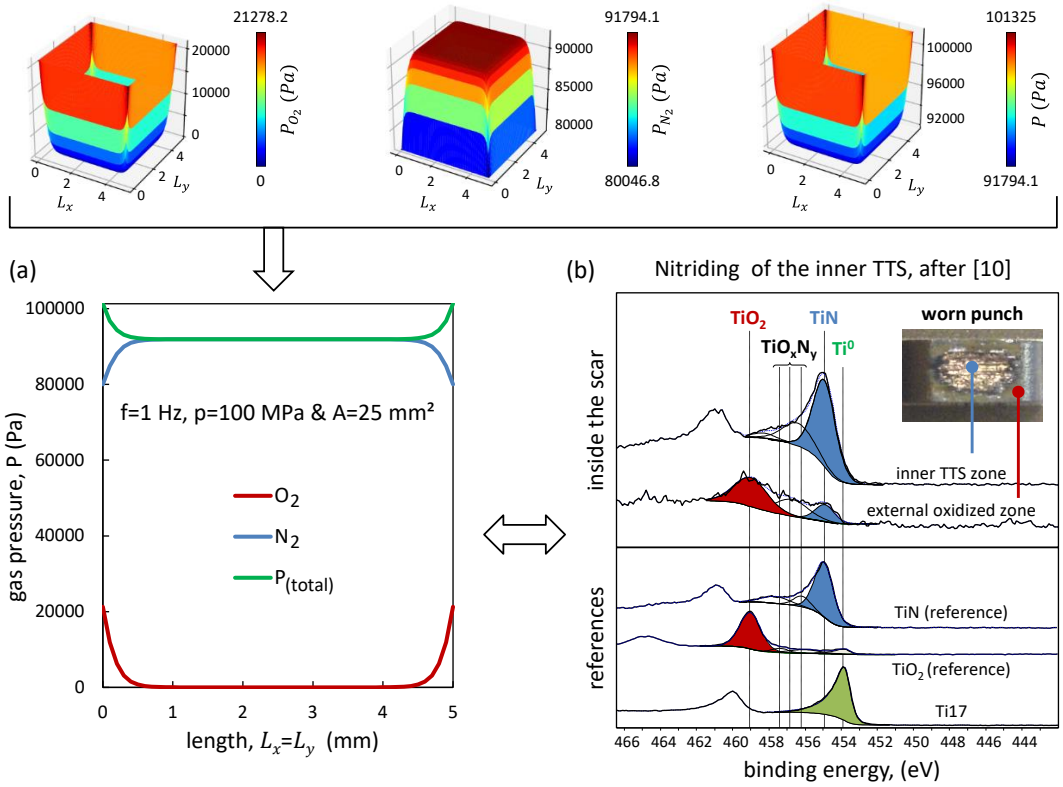

Fig. 24. (a) 2D and 3D graphs showing the evolution of the partial pressures of oxygen and nitrogen gases along with the total pressure within the debris bed at the reference test; (b) XPS spectra of the inner adhesion zone and the surrounding oxidized abrasion corona giving evidence of Ti17 nitriding inside the TTS (after [10]).

On the other hand, by depriving oxygen and in turn increasing the concentration of nitrogen gas, such air distilling process presently modelled using ADR approach can explain the nitriding process observed in many closed fretting interfaces.

The given ADR approach appears as an interesting strategy to better predict the fretting wear phenomenon taking into account the tribo-oxidation processes operating within the interface. However, the present formulation is a first step which can be improved in many aspects to better formalize the effect of materials and contact loadings.

For instance, the given formulation does not consider the worn contact area extension classically observed for Hertzian contacts. Future developments are now required to combine both surface wear and ADR analyses in order to generalize this approach for usual sphere-on-flat and cylinder-on-flat fretting contacts.

The model considers a steady state description which was a posteriori confirmed by experiments where oxygen distance d_O stabilizes after few hundred hundreds of cycles [14]. However, there is a key interest to take into account the transient period particularly for a non-conformal Hertzian contacts showing variation in contact area and contact pressure.

This analysis must be also extended to other materials like titanium or bronze alloys to establish how their surface reactivity can influence adhesive wear extension and to check how the ADR model will capture such evolutions.

This material analysis should also be correlated with environmental investigations [46,55]. Indeed, by performing fretting wear tests under variable oxygen partial pressure conditions, it will be possible to verify the stability of the ADR approach to predict the

oxygen distance and consequently adhesive wear extension. This helps better quantify the $P_{O_2,th}$ threshold values as a function of the studied materials.

As said previously, the model can be further ameliorated by better formalizing the effect of the contact pressure which not only affects the oxygen consumption rate through friction power dissipation but also the porosity and the permeability of the debris bed.

Similar investigation must be undertaken regarding the effect of sliding amplitude whose role is not yet well understood in literature as it contributes not only in friction work dissipation but also on the ejection of the third body particles [59] which affect the intrinsic properties of the porous debris bed.

Hence, investigating and modelling all these aspects through a combined surface wear and ADR approach, appears as a challenging scientific project which will constitute our main objective in future investigations.

7. Conclusion

The purpose of this research work is to explain and model contact oxygenation observed in fretting contacts. This achieved by modelling oxygen transport using an advection-dispersion-reaction (ADR) approach by considering debris bed as compact powdery porous medium traversed by two gases: oxygen and nitrogen. From these investigations, the following points can be outlined:

-Using this ADR model, it was possible to predict the so-called oxygen distance (d_O) marking the transition between abrasive wear area in the outer part of the fretting scar and the adhesive wear area (i.e. metal transfer) observed in the inner part of the contact.

-ADR model, which was calibrated using only three fretting tests at different frequencies, was able to predict wide range of experimental conditions including sliding frequency, contact pressure and contact size. This, a posteriori, confirms the stability of this approach.

-Sensitivity analysis dedicated to study debris bed properties pointed out that the controlling factor of the interface properties is the porosity parameter. In the present investigation, a constant porosity value was assumed. Despite the simplicity of this hypothesis, good predictions were achieved. However, future investigations should be undertaken to better formalize this parameter taking into account, for instance, the effect of the contact pressure.

-The reaction rate coefficient of the model was formalized using a basic power-law formulation involving Archard power density factor. Although it is simple, the good prediction obtained using this approximation suggests that the Archard power density parameter (i.e. p.v factor) seems to be a pertinent physical variable to formalize the reaction rate and finally predict the oxygen distance.

-ADR model was validated at different sliding frequencies, contact pressures and contact sizes. Nevertheless, it still needs to be extended in future development to capture the effect of the sliding amplitude and metal reactivity.

To conclude, despite its simplicity, the given ADR model provides, for the first time, a quantitative description of the contact oxygenation concept (COC) and appears as a challenging strategy to develop future multi-physical modelling of fretting wear processes.

Acknowledgement

The authors gratefully acknowledge the French National Research Agency (ANR, France) and the Ecole Centrale de Lyon (ECL, France) for financially supporting this research project (ANR-16-CE08-0016). Additionally, thanks are extended to Julie Laporte and Jean-Michel Vernet for their technical help.

References

[1] O. Vingsbo, S. Soderberg, On fretting maps, Wear. 126 (1988) 131–147. doi:10.1016/0043-1648(88)90134-2.

[2] P.L. Hurricks, The fretting wear of mild steel from room temperature to 200°C, Wear. 19 (1972) 207–229. doi:10.1016/0043-1648(72)90304-3.

[3] D. Tabor, Wear–A Critical Synoptic View, J. Lubr. Technol. 99 (2010) 387. doi:10.1115/1.3453231.

[4] P.L. Hurricks, Some metallurgical factors controlling the adhesive and abrasive wear resistance of steels. A review, Wear. 26 (1973) 285–304. doi:10.1016/0043-1648(73)90184-1.

[5] J. John T. Burwell, Survey of possible wear mechanisms, Wear. 1 (1957) 119–141. doi:10.1016/0043-1648(57)90005-4.

[6] E. Sauger, S. Fouvry, L. Ponsonnet, P. Kapsa, J.. Martin, L. Vincent, Tribologically transformed structure in fretting, Wear. 245 (2000) 39–52. doi:10.1016/s0043-1648(00)00464-6.

[7] V. Nurmi, J. Hintikka, J. Juoksukangas, M. Honkanen, M. Vippola, A. Lehtovaara, A. Mäntylä, J. Vaara, T. Frondelius, The formation and characterization of fretting-induced degradation layers using quenched and tempered steel, Tribol. Int. 131 (2019) 258–267. doi:10.1016/j.triboint.2018.09.012.

[8] S. Descartes, Y. Berthier, Rheology and flows of solid third bodies: Background and application to an MoS1.6coating, Wear. 252 (2002) 546–556. doi:10.1016/S0043-1648(02)00008-X.

[9] S. Fouvry, P. Arnaud, A. Mignot, P. Neubauer, Contact size, frequency and cyclic normal force effects on Ti–6Al–4V fretting wear processes: An approach combining friction power and contact oxygenation, Tribol. Int. 113 (2017) 460–473. doi:10.1016/j.triboint.2016.12.049.

[10] C. Mary, S. Fouvry, J.M. Martin, B. Bonnet, Pressure and temperature effects on Fretting Wear damage of a Cu-Ni-In plasma coating versus Ti17 titanium alloy contact, Wear. 272 (2011) 18–37. doi:10.1016/j.wear.2011.06.008.

[11] A.R. Warmuth, S.R. Pearson, P.H. Shipway, W. Sun, The effect of contact geometry on fretting wear rates and mechanisms for a high strengthsteel, Wear. 301 (2013) 491–500. doi:10.1016/j.wear.2013.01.018.

[12] X. Jin, P.H. Shipway, W. Sun, The role of frictional power dissipation (as a function of frequency) and test temperature on contact temperature and the subsequent wear behaviour in a stainless steel contact in fretting, Wear. 330–331 (2015) 103–111. doi:10.1016/j.wear.2015.02.022.

[13] A.R. Warmuth, P.H. Shipway, W. Sun, Fretting wear mapping: The influence of contact geometry and frequency on debris formation and ejection for a steel-on-steel pair, Proc. R. Soc. A Math. Phys. Eng. Sci. 471 (2015). doi:10.1098/rspa.2014.0291.

[14] S. Baydoun, S. Fouvry, An experimental investigation of adhesive wear extension in fretting interface: Application of the contact oxygenation concept, Tribol. Int. 147 (2020) 106266. doi:10.1016/j.triboint.2020.106266.

[15] H.T. Abuluwefa, R.I.L. Guthrie, F. Ajersch, Oxidation of low carbon steel in multicomponent gases: Part I. Reaction mechanisms during isothermal oxidation, Metall. Mater. Trans. A Phys. Metall. Mater. Sci. 28 (1997) 1633–1641. doi:10.1007/s11661-997-0255-7.

[16] H.T. Abuluwefa, Kinetics of high temperature oxidation of high carbon steels in multi-component gases approximating industrial steel reheat furnace atmospheres, Lect. Notes Eng. Comput. Sci. 2196 (2012) 1664–1668.

[17] T.J. Benham, E.R. Leheup, J.R. Moon, The effect of debris chemistry on the debris formation and fretting behaviour of mild steel in CO2 containing oxygen and water vapour, Wear. 177 (1994) 195–202. doi:10.1016/0043-1648(94)90245-3.

[18] V.B. Stein, J.P.A. Hettiaratchi, G. Achari, Numerical model for biological oxidation and migration of methane in soils, Pract. Period. Hazardous, Toxic, Radioact. Waste Manag. Am. Soc. Civ. Eng. 5 (2001) 225–234. doi:10.1061/(ASCE)1090-025X(2001)5:4(225).

[19] H. Darcy, Les fontaines publiques de la ville de Dijon, V. Dalamont, 1856.

[20] C.K. Ho, S.W. Webb, Gas Transport in Porous Media, 2006. doi:10.1017/S0022112000211312.

[21] J. Dalton, New theory of the constitution of mixed gases elucidated, Philos. Mag. 14 (1802) 169–173. doi:10.1080/14786440208676179.

[22] C.R. Wilke, A viscosity equation for gas mixtures, J. Chem. Phys. 18 (1950) 517–519. doi:10.1063/1.1747673.

[23] J. Kozeny, Uber kapillare leitung der wasser in boden, R. Acad. Sci. Vienna, Proc. Cl. I. 136 (1927) 271–306.

[24] P.C. Carman, Flow of gases through porous media, Butterworths Scientific Publications, 1956.

[25] M.S. Costanza-Robinson, M.L. Brusseau, Gas-Phase Dispersion in Porous Media, in: Gas Transp. Porous Media, 2006: pp. 121–132. doi:10.1007/1-4020-3962-x_7.

[26] A. Fick, Ueber Diffusion, Ann. Phys. 170 (1855) 59–86. doi:https://doi.org/10.1002/andp.18551700105.

[27] D.F. Fairbanks, C.R. Wilke, Diffusion Coefficients in Multicomponent Gas Mixtures, Ind. Eng. Chem. 42 (1950) 471–475. doi:10.1021/ie50483a022.

[28] N.H. Chen, D.F. Othmer, New Generalized Equation for Gas Diffusion Coefficient, J. Chem. Eng. Data. 7 (1962) 37–41. doi:10.1021/je60012a011.

[29] A. Kia, H.S. Wong, C.R. Cheeseman, Clogging in permeable concrete: A review, J. Environ. Manage. 193 (2017) 221–233. doi:10.1016/j.jenvman.2017.02.018.

[30] T. Moldrup, P and Kruse, CW and Rolston, DE and Yamaguchi, Modeling diffusion and reaction in soils: III. Predicting gas diffusivity from the Campbell soil-water retention model, Soil Sci. 161 (1996) 366–375. doi:10.1097/00010694-199606000-00003.

[31] D. Werner, P. Grathwohl, P. Höhener, Review of Field Methods for the Determination of the Tortuosity and Effective Gas-Phase Diffusivity in the Vadose Zone, Vadose Zo. J. 3 (2004) 1240–1248. doi:10.2136/vzj2004.1240.

[32] M.S. Costanza-Robinson, M.L. Brusseau, Gas phase advection and dispersion in unsaturated porous media, Water Resour. Res. 38 (2002) 7-1-7–9. doi:10.1029/2001wr000895.

[33] P.J. Binning, D. Postma, T.F. Russell, J.A. Wesselingh, P.F. Boulin, Advective and diffusive contributions to reactive gas transport during pyrite oxidation in the unsaturated zone, Water Resour. Res. 43 (2007) 1–12. doi:10.1029/2005WR004474.

[34] J.F. Pickens, G.E. Grisak, Scale-dependent dispersion in a stratified granular aquifer, Water Resour. Res. 17 (1981) 1191–1211. doi:10.1029/WR017i004p01191.

[35] C. Mary, T. Le Mogne, B. Beaugiraud, B. Vacher, J.M. Martin, S. Fouvry, Tribochemistry of a Ti alloy under fretting in air: Evidence of titanium nitride formation, Tribol. Lett. 34 (2009) 211–222. doi:10.1007/s11249-009-9426-6.

[36] E. Clapeyron, Mémoire sur la puissance motrice de la chaleur, J. l'École Polytech. 14 (1834) 153–190.

[37] S. Baydoun, S. Fouvry, S. Descartes, P. Arnaud, Fretting wear rate evolution of a flat-on-flat low alloyed steel contact: A weighted friction energy formulation, Wear. 426–427 (2019) 676–693. doi:10.1016/j.wear.2018.12.022.

[38] S. Fouvry, H. Gallien, B. Berthel, From uni- to multi-axial fretting-fatigue crack nucleation: Development of a stress-gradient-dependent critical distance approach, Int. J. Fatigue. 62 (2014) 194–209. doi:10.1016/j.ijfatigue.2013.05.016.

[39] A.R. Moustafa, Mesure thermographique des effets dissipatifs accompagnant le fretting : d'une construction rapide des cartes d'amorçage vers une meilleure comprehension des mecanismes d'endommagement, PhD thesis, Ecole Centrale de Lyon, 2016.

[40] G. Straffelini, A. Molinari, Dry sliding wear of Ti – 6Al – 4V alloy as influenced by the counterface and sliding conditions, Wear. 236 (1999) 328–338.

[41] T. Jibiki, M. Shima, H. Akita, M. Tamura, A basic study of friction noise caused by fretting, Wear. 251 (2001) 1492–1503.

[42] J.S. Halliday, W. Hirst, The fretting corrosion of mild steel, Proc. R. Soc. London. Ser. A. Math. Phys. Sci. 236 (1956) 411–425. doi:10.1098/rspa.1956.0145.

[43] P.L. Hurricks, The mechanism of fretting-A review, Wear. 15 (1970) 389–409. doi:doi:https://doi.org/10.1016/0043-1648(70)90235-8.

[44] D.G. Poitout, Biomechanics and Biomaterials in Orthopedics, Springer London, 2004.

[45] B. Bhushan, Principles and Applications of Tribology, Second Edition, 2013.

[46] Y. Zhang, G. Mollon, S. Descartes, Significance of third body rheology in friction at a dry sliding interface observed by a multibody meshfree model: Influence of cohesion between particles, Tribol. Int. 145 (2020) 106188. doi:10.1016/j.triboint.2020.106188.

[47] A.M. Kirk, P.H. Shipway, W. Sun, C.J. Bennett, Debris development in fretting contacts – Debris particles and debris beds, Tribol. Int. (2019) 1–9. doi:10.1016/j.triboint.2019.01.051.

[48] L. Blades, D. Hills, D. Nowell, K.E. Evans, C. Smith, An exploration of debris types and their influence on wear rates in fretting, Wear. 450–451 (2020) 203252. doi:10.1016/j.wear.2020.203252.

[49] A.B. Yu, R.P. Zou, Prediction of the porosity of particle mixtures, KONA Powder Part. J. 16 (1998) 68–81. doi:10.14356/kona.1998010.

[50] N. Ouchlyama, T. Tanaka, Porosity estimation from particle size distribution, Ind. Eng. Chem. Fundam. 25 (1986) 125–129. doi:10.1021/i100021a019.

[51] P. Glover, Petrophysics, Department of Geology and Petroleum Geology, University of Aberdeen Uk, 2000.

[52] K.H. Roscoe, A.N. Schofield, C.P. Wroth, On the yielding of soils, Geotechnique. 8 (1958) 22–53. doi:10.1680/geot.1958.8.1.22.

[53] D. Poquillon, J. Lemaitre, V. Baco-Carles, P. Tailhades, J. Lacaze, Cold compaction of iron powders - Relations between powder morphology and mechanical properties: Part I: Powder preparation and compaction, Powder Technol. 126 (2002) 65–74. doi:10.1016/S0032-5910(02)00034-7.

[54] A.S. Khanna, Introduction to high temperature oxidation and corrosion, ASM international,

2002.

[55] A. Iwabuchi, T. Kayaba, K. Kato, Effect of atmospheric pressure on friction and wear of 0.45% C steel in fretting, Wear. 91 (1983) 289–305. doi:10.1016/0043-1648(83)90074-1.

[56] J.F. Archard, Contact and rubbing of flat surfaces, J. Appl. Phys. 24 (1953) 981–988. doi:10.1063/1.1721448.

[57] D. Bowden, F. P. Tabor, The friction and lubrication of solids, Oxford university press, 1950.

[58] A.M. Kirk, P.H. Shipway, W. Sun, C.J. Bennett, The effect of frequency on both the debris and the development of the tribologically transformed structure during fretting wear of a high strength steel, Wear. 426–427 (2019) 694–703. doi:10.1016/j.wear.2018.12.035.

[59] A. Dreano, S. Fouvry, G. Guillonneau, Understanding and formalization of the fretting-wear behavior of a cobalt-based alloy at high temperature, Wear. 452–453 (2020) 203297. doi:10.1016/j.wear.2020.203297.